Chapter 13
Syntheses and Applications of Silver Halide-Based Photocatalysts

13.1 Introduction

In the past decades, photocatalysis has received increasing attention for its potential to solve worldwide energy crisis (water splitting [1–4] and solar cell [5–7]), environmental pollution (water and air purification [8–12], and pathogen inactivation [13–15]), and greenhouse effect (CO_2 conversion [16–19]). Among various photocatalytic materials, TiO_2 has been the most widely researched for its excellent properties, such as high photocatalytic activity, low cost, high stability, and nontoxicity [20–24]. However, its two defects, no response to visible light and low photo-quantum efficiency, seriously limit its practical application. Hence, to full use of solar energy, the development of visible light-driven photocatalytic materials has become the most significant topic in the photocatalytic field.

Silver halide (AgX), a kind of well-known photographic material, was developed in 1839 with the daguerreotype [25, 26]. The photographic process in AgX is as follows: after absorbing a photon, silver halide can produce an electron and a hole, and subsequently the electron combines with an interstitial silver ion to form an Ag^0 atom [27, 28]. Upon repeated absorption of photons, a cluster of silver atoms (latent image) will be formed ultimately [29, 30]. Due to the instability under light, silver halides are seldom used as photocatalysts previously.

In 1996, the photocatalytic activity of AgX was firstly reported by Calzaferri et al. [31]. During the photocatalytic reaction, the photo-generated electron–hole pairs will react with sacrificial agent and water to evolve O_2 or H_2. In this period, the Ag nanoparticles formed on the surface of AgX were seen as electron trappers, which can capture photo-generated electrons by Schottky barrier between Ag and AgX. Therefore, the formation of Ag nanoparticles can not only enhance the photocatalytic activity of AgX by separating carriers but also improve the stability of AgX by decreasing the amount of electrons in AgX [32]. In 2008, Huang et al. [33] found that the Ag nanoparticles on AgX can also enhance the absorption of visible light by surface plasma resonance (SPR) effect, which triggered an upsurge

Fig. 13.1 (**A**) Crystal, structure, and lattice parameter of AgCl, AgBr, and AgI. (**B**) The models of face-centered cubic crystal

(A)

Name	Crystal	Sturcture	Lattice paramater a (Å)
AgCl	fcc	rock-salt	5.5491
AgBr	fcc	rock-salt	5.7745
AgI(α)	fcc	rock-salt	6.4950

(B)
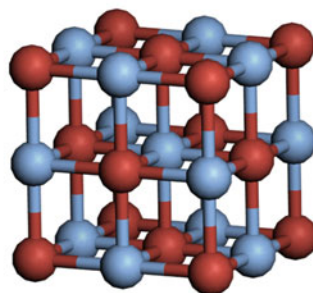
of researching Ag/AgX plasmonic photocatalysts. So far, a large number of researches involved in AgX have been carried out, including the morphology control, establishment of heterojunction or Z-scheme structure, and combining with recoverable material.

In this chapter, we will firstly introduce the properties and synthesis strategies of AgX materials and the preparation and characteristic of AgX with different morphologies. After that, the AgX-based heterojunction and Z-scheme structures will be classified by different composites and band structure, and each type will be presented detailedly. Finally, the present researches of recoverable AgX materials will be introduced.

13.2   Properties of AgX

AgCl, AgBr, and AgI(α) are face-centered cubic (fcc) crystal and rock salt (NaCl) structure, as shown in Fig. 13.1a, and their lattice parameters are 5.5491, 5.7745, and 6.4950 Å, respectively [34]. In detail, as shown in Fig. 13.1b, the Ag and Br atoms are all sixfold coordinated by Br and Ag atoms in the crystal. The solubility of AgCl, AgBr, and AgI(α) in water is extremely low. The Ksp for AgCl, AgBr, and AgI(α) are 1.77×10^{-10}, 5.35×10^{-13}, and 8.52×10^{-17}, respectively. The optical properties of AgCl, AgBr, and AgI(α) are dependent on their band gap. According to the literatures, the indirect band gaps of AgCl, AgBr, and AgI(α) are 3.30 [35], 2.65 [36], and 2.80 eV [37], respectively (Table 13.1). It should be noticed that the band gap of AgCl is over 2.95 eV, indicating that it can only absorb UV light. However, the Ag$^+$ on the surface of AgCl is easily reduced to Ag^0, which not only responds to visible light by SPR effect but also enhances the stability of AgCl via capturing photo-generated electrons.

Table 13.1 CB level, VB level, and band gap of AgCl, AgBr, and AgI(α)

Name	CB level (eV)	VB level (eV)	Band gap (eV)
AgCl	-1.20	2.10	3.30
AgBr	-0.50	2.15	2.65
AgI(α)	-0.42	2.38	2.80

Fig. 13.2 Illustration of the nucleation and growth of AgX crystal during precipitation process, in which C_s is the solubility while C^*_{min} and C^*_{max} are the minimum and maximum concentration of nucleation, respectively
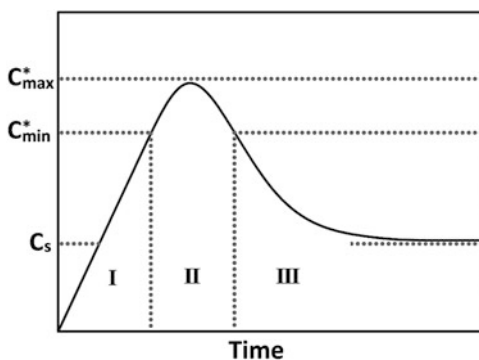
13.3   Synthesis Strategies

In past 20 years, many methods have been developed to prepare AgX photocatalytic materials. Most of these methods are mainly based on the extremely low solubility of AgX. Generally, these methods can be classified into three synthesis strategies: liquid–solid precipitation, in situ oxidation transformation, and ion exchange.

13.3.1   Liquid–Solid Precipitation

As we all know, in an aqueous solution, the activities of Ag ions [Ag$^+$] and X ions [X$^-$] are related to the solubility product K$_{sp}$ ([Ag$^+$] [X$^+$] = K$_{sp}$). The relation between ion concentration and precipitation process of AgX is described in Fig. 13.2, in which C_s, C^*_{min}, and C^*_{max} represented the concentration corresponding to solubility, the critical supersaturation (the minimum concentration of nucleation), and the limiting supersaturation (the maximum concentration of nucleation), respectively. At the initial stage of adding Ag$^+$ and X$^-$ ions (Stage I), no AgX nucleus can be formed because the concentration is below C^*_{min}. When the concentration exceeds C^*_{min} (Stage II), with the continuous addition of Ag$^+$ and X$^-$, the spontaneous nucleation of AgX takes place rapidly and the concentration begins to decrease. When the concentration is below C^*_{min} but higher than C_s (Stage III), the nucleation of AgX ceases and the AgX crystal nuclei grow gradually with the continuous addition of Ag$^+$ and X$^-$ ions. In order to control the uniformity of crystal size, it is important to keep the concentration lower than C^*_{min} after the initial nucleation finished to prevent the occurrence of further nucleation.
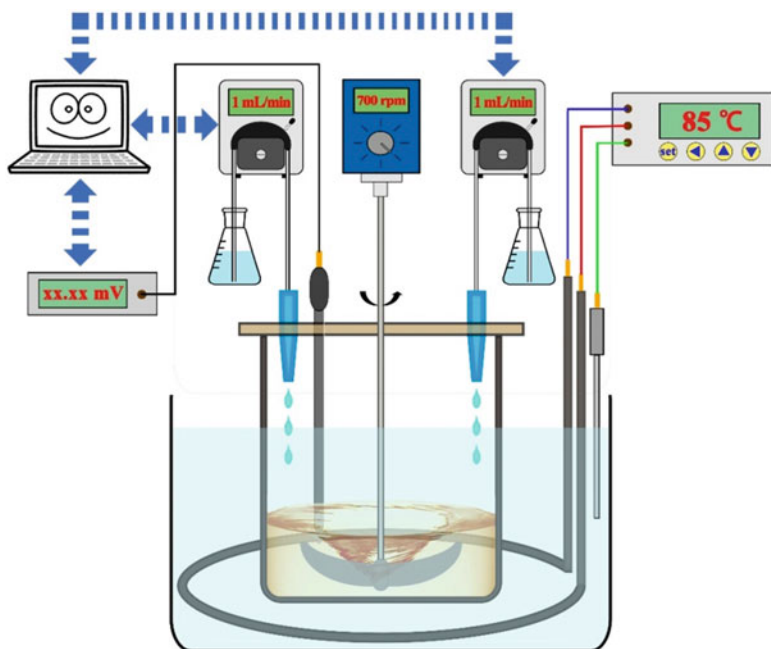
Fig. 13.3 Illustration of the apparatus for double-jet precipitation

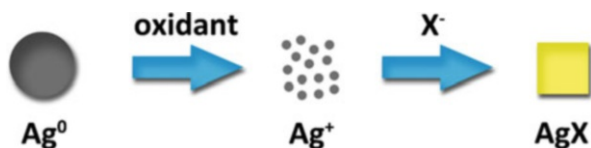**Fig. 13.4** Illustration of in situ oxidation transformation process

Figure 13.3 illustrates the computer-controlled double-jet precipitation apparatus for preparing AgBr crystals, by which the concentration of Ag^+ and X^- during the whole precipitation process can be precisely controlled [38–40]. As displayed in Fig. 13.3, the concentrations of Ag^+ and X^- ions are detected by ion selective electrodes and the injecting rates of Ag^+ and X^- ions are adjusted on the basis of the detecting results. Beneficial from this apparatus, the concentration can be controlled to below the C^*_{min} after nucleation process to control the uniformity of crystal size. By the double-jet precipitation apparatus, AgCl and AgBr crystals with different morphologies have been successfully synthesized [36, 41–44].

13.3.2 In Situ Oxidation Transformation

Different to the liquid–solid precipitation, the Ag source used in oxidation transformation is usually metallic silver (Ag^0) [45]. As shown in Fig. 13.4, the oxidant is

Fig. 13.5 Illustration of ion exchange process

added into the reaction system to oxide Ag^0 and release Ag^+. The released Ag^+ ions further react with X^- ions immediately to form AgX particles in situ. The advantage of this synthesis strategy is easily combining AgX with other semiconductors or substrates, because it is much easier to form Ag^0 on the surface of other materials than to directly form AgX.

13.3.3   Ion Exchange

According to the kind of exchanged ion, this synthetic strategy can be divided into cation exchange and anion exchange. During cation exchange process, the halide salts (MX) are used as the X sources. Then, Ag^+ will replace M^+ in MX due to the extremely low solubility of AgX and from AgX. Similarly, in the case of anion exchange process, the silver salts (AgY) acts as Ag sources. And X^- will exchange with Y^- in AgY. By this strategy, the obtained AgX can keep the original morphology of its precursor MX or AgY (Fig. 13.5).

13.4   Synthesis and Application of AgX with Different Morphologies

Morphology is a significant factor that influences the photoelectrochemical and photocatalytic performances of photocatalytic materials. As for AgX photocatalysts, the reported morphologies mainly include 1D, 3D, facet exposed, and porous structures.

13.4.1   1D Structure

Compared with bulk materials, one dimensional (1D) structured semiconductor materials, including nanowires, nanorods, nanotubes, and nanobelts, usually exhibit better electronic, optoelectronic, and electromechanical properties. These excellent properties will directly cause the enhancement in photocatalytic performances. In the past decades, several kinds of AgX-based 1D materials have been reported. In these works, there exist two synthetic strategies: (a) oxidation–halogenation method and (b) wet chemical method with dissolution and recrystallization progress.
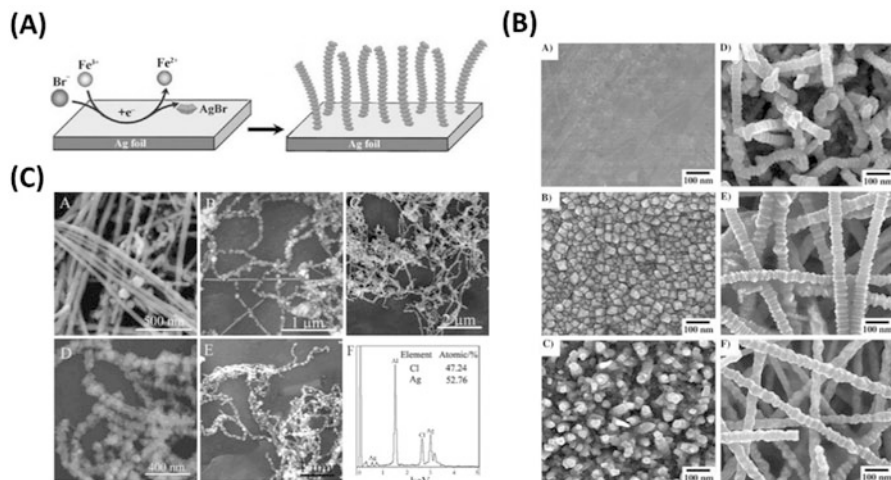
Fig. 13.6 (**a**) Schematic illustration of the heteroepitaxial growth process of AgBr nanowires on Ag substrates; (**b**) SEM images of AgBr nanowires during growth process at different reaction times (0, 0.5, 1, 2, 4, and 6 h) [46]. Reproduced from Ref. [46] by permission of John Wiley & Sons Ltd. (**c**) SEM images of the necklace-like Ag/AgCl nano-heterostructures with different AgCl amount (10%, 30%, 80%, 85%, and 100%) and EDS analysis of Ag/AgCl with 85% AgCl [50]. (Reproduced from Ref. [50] by permission of John Wiley & Sons Ltd)

1. *Oxidation–Halogenation Method*

Metallic Ag with different morphologies, foil, nanowire, or nanotube, can be utilized as the Ag source. In the oxidation–halogenation processes, an oxidation reaction (Ag^0 + oxidant → Ag^+ + reductant) and a halogenation reaction ($Ag^+ + X^-$ → AgX) will occur together.[46–54] Firstly, metallic Ag is oxidized into Ag^+ ion in the presence of oxidant such as Fe^{3+} or H_2O_2. Meanwhile, the dissolved X^- ion immediately combines with the released Ag^+ ion to form AgX. For example, Ye et al. largely synthesized uniform AgBr nanowires using commercial silver foils at room temperature [46]. It was revealed that the towerlike AgBr nanowire was produced by the following pathway: Firstly, the uniform AgBr nanocrystals with octahedron-like structures formed tidily on the surfaces of Ag foils. Then, with prolonging the reacting time, the formed AgBr nanocrystals attached to each other and self-assembled into towerlike nanostructure arrays under the direction of PVP (Fig. 13.6a, b). Using Ag nanowires as Ag source and $FeCl_3$ as oxidant, Huang et al. fabricated necklace-like Ag/AgCl nano-heterostructures [50]. By adjusting the addition of $FeCl_3$, the amount of AgCl in Ag/AgCl nanowires can be conveniently controlled, in Fig. 13.6c. They found that the ratio of Ag and AgCl plays an important role in determining the photocatalytic activity of Ag/AgCl nanowires. When the ratio of AgCl and Ag is 85:15, the Ag/AgCl nanowires exhibit the optimal photocatalytic activity for the decomposition of organic pollutants and water splitting to produce oxygen.
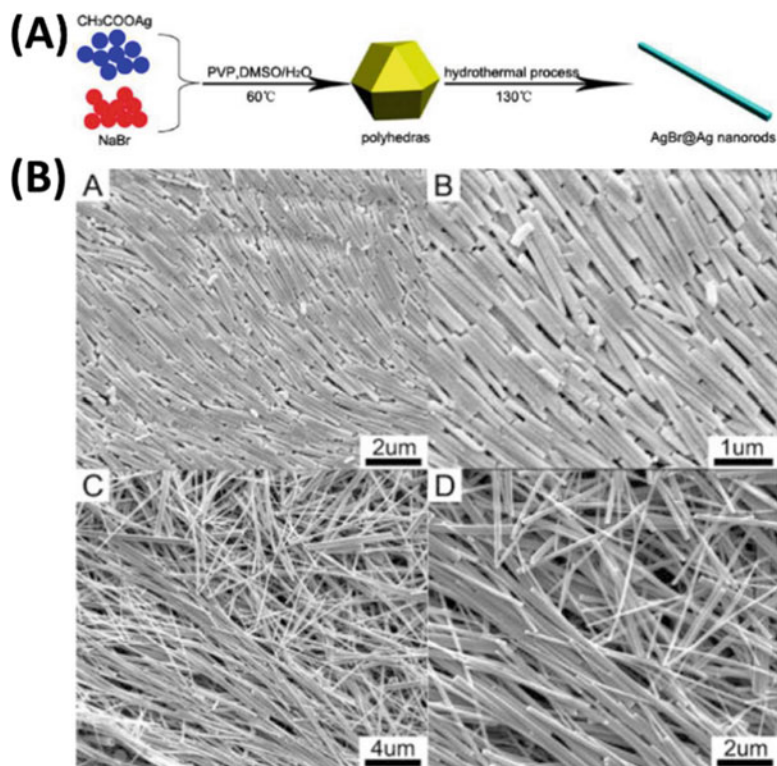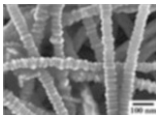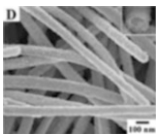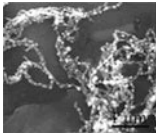
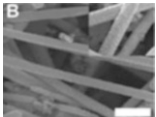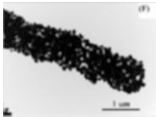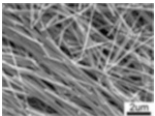**Fig. 13.7** (**a**) Schematic illustration for the formation of the AgBr@Ag nanorods; (**b**) SEM images of AgBr@Ag nanorods and nanowires at low and high magnification, respectively [55]. (Reprinted with the permission from Ref. [55]. Copyright 2013 American Chemical Society)

2. *Dissolution and Recrystallization Processes*

1D AgBr nanowires and nanorods can also be prepared by the two-step processes: dissolution and recrystallization [55]. As illustrated in Fig. 13.7a: Firstly, AgBr nanocrystallines were prepared by dropping CH_3COOAg water solution into NaBr mixture solution ($DMSO/H_2O= 1:2$). Then, the above suspension was directly added into autoclave for hydrothermal treatment. During the hydrothermal process, AgBr nanocrystallines act as the crystal seeds to form 1D structure by dissolution and recrystallization. In this process, both DMSO and PVP are indispensable for the formation of 1D structure. The former can not only enhance the dissolution of AgBr but also stabilize the AgBr {111} facets by interacting with the positively charged "Ag" with polarized functional group "−S=O." The latter can also absorb on the {111} facets of AgBr by "−C=O" to increase the exposure of {111} facets. From Fig. 13.7b, it can be seen that the AgBr nanorods can be changed to AgBr nanowires by slightly changing the experiment condition [55].

(a) Oxidation–halogenation method

Reactant	Oxidizing agent	Halide source	Parameter control	Morphology	References
Ag foil	$Fe(NO_3)_3$	NaBr	Reaction time	Towerlike AgBr nanowire	[46]
Ag nanowire	$FeCl_3$	$FeCl_3$	Reaction time	Ag/AgCl core–shell nanowire	[48] [49]
Ag nanowire	$FeCl_3$	$FeCl_3$	Quantity of $FeCl_3$	Necklace-like Ag/AgCl nanowire	[50] [51] [52]
Ag nanowire	H_2O_2	HCl		Ag/AgCl nanowire	[53]
Ag nanotube	$FeCl_3$	$FeCl_3$	Quantity of $FeCl_3$	Ag@AgCl nanotube	[54]

(b) Dissolution and recrystallization progress

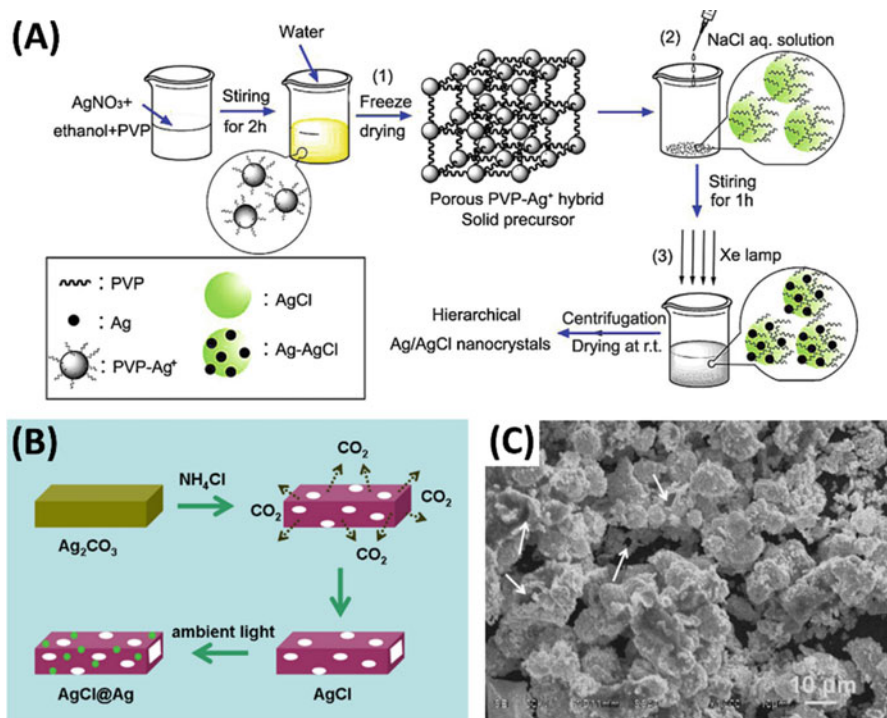| Reactant	Reacting condition	Parameter control	Morphology	Reference
AgAc and NaBr	1. PVP, DMSO/H_2O 60 °C	1. Hydrothermal treatment time	AgBr@Ag nanowire	[55]
	2. Hydrothermal treatment 130 °C	2. Ratio of DMSO/H_2O		

Fig. 13.8 Schematic diagram for the synthesis of (**a**) hierarchical Ag/AgCl nanocrystals via a freeze-drying route.[56] Reprinted from Ref. [56], Copyright 2014, with permission from Elsevier. (**b**) AgCl@Ag hollow architectures; (**c**). SEM images of AgCl@Ag hollow architectures [57]. (Reprinted from Ref. [57], Copyright 2013, with permission from Elsevier)

13.4.2   3D Structure

Different to the 1D structured AgX, 3D structured AgX have more complex framework. This framework can not only increase the surface area to provide more active sites but also promote the transfer of reactants from outside to inside. So far, the strategies for synthesizing AgX 3D structure can be classified into three types:

1. *Anion Exchange Method*

   Anion exchange method is one of the effective routes to prepare 3D AgX-based photocatalysts. For this method, the formation mechanism of AgX is based on the principle that the solubility of AgX is lower than that of their precursor Ag salts. For example, Chen et al. firstly synthesized porous PVP–Ag$^+$ hybrid compounds by a freeze-dying route (Fig. 13.8a). Then, the obtained PVP–Ag$^+$ were transformed to hierarchical Ag/AgCl nanocrystals through a liquid–solid precipitation reaction with addition of NaCl solution. The photocatalytic performance of hierarchical Ag/AgCl nanocrystals was higher than that of P25 for the photo-degradation of organic dyes
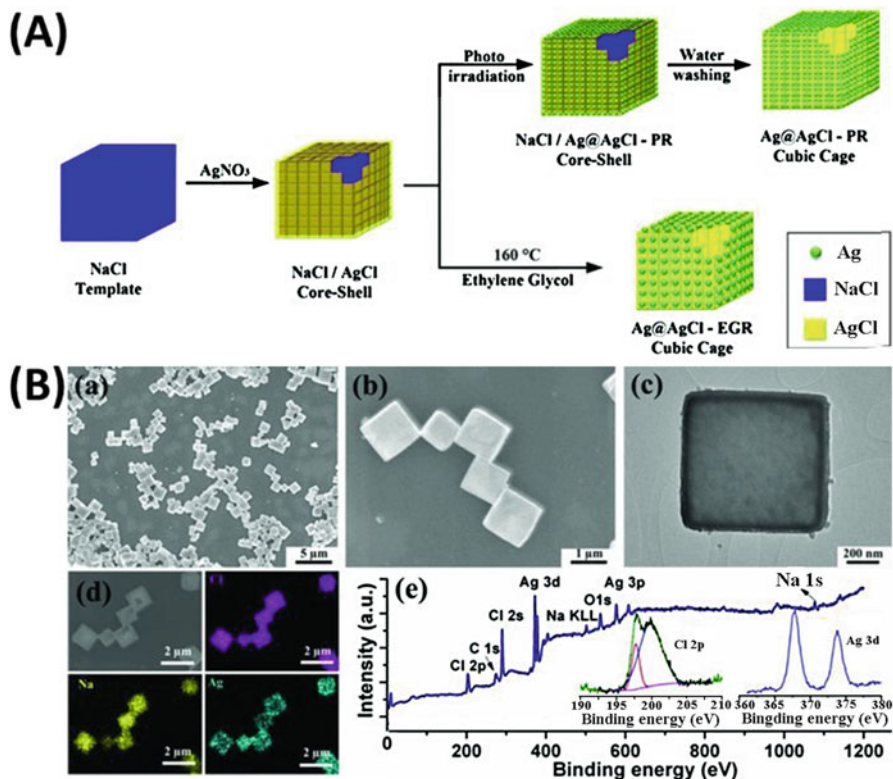
Fig. 13.9 (**a**) Schematic illustration of the water-soluble sacrificial salt–crystal–template (SCT) route for the formation of Ag@AgCl cubic cages. Two methods have been selected to generate Ag NPs: photoreduction (PR) and ethylene glycol-assisted reduction (EGR); (**b**). (*a, b*) Typical FESEM images of NaCl/AgCl core–shell cubes. (*c*) TEM image of an individual NaCl/AgCl core–shell cube [58]. (Reproduced from Ref. [58] by permission of John Wiley & Sons Ltd)

(RhB, MO, and MB) and alcohols (methanol and isopropanol) under visible light. [56] Similarly, Jiang et al. prepared AgCl@Ag hollow architectures by employing NH_4Cl as a reactive acidic etching agent to etch Ag_2CO_3 particles (Fig. 13.8b).[57] During the etching process, the surface of Ag_2CO_3 would be chlorinated and the poles would be created. Finally, the hierarchical porous AgCl@Ag hollow architectures were formed (Fig. 13.8c). The obtained hierarchical porous structure not only increases the adsorption of contaminants but also enhances the harvesting efficiency of light.

2. *Cation Exchange Method*

Similar to anion exchange method, the difference of solubility between AgX and MX (M means other metal element) is also used in cation exchange method. Different to the former method, the MX used in cation exchange method is usually with uniform morphology, such as cube and sphere. Consequently, the morphology of prepared 3D AgX is usually regular [58–62]. For instance, Chen et al. [58] prepared AgCl cubic cages using cubic NaCl crystals as a water-soluble sacrificial
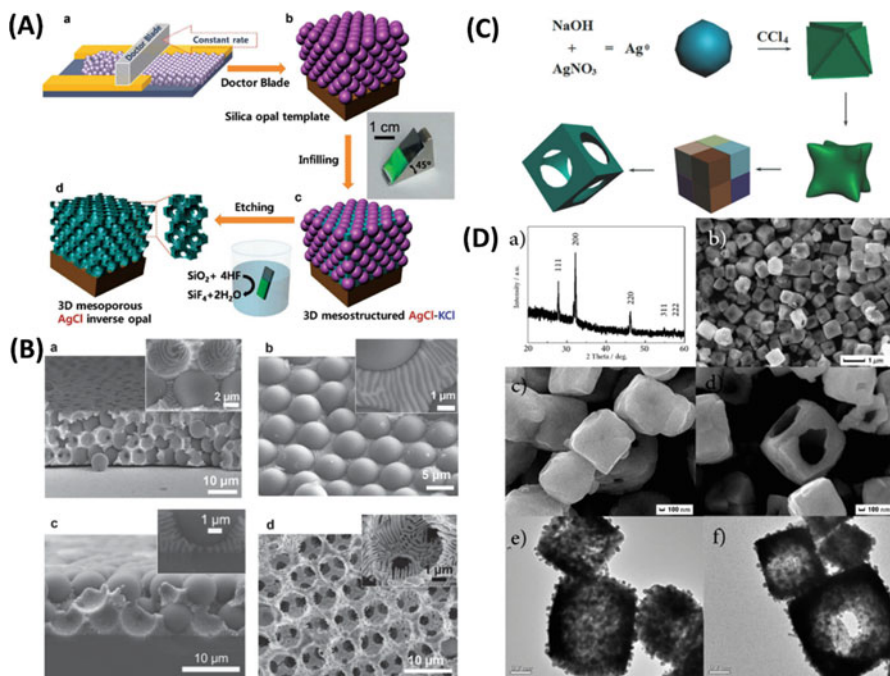
Fig. 13.10 (**a**) Key steps for fabricating 3D mesostructured AgCl–KCl and 3D mesoporous AgCl inverse opal structure; (**b**) SEM images of the air-cooled AgCl–KCl eutectic templated by colloid template. (*a*) cross-sectional, (*b*) plan view, (*c*) a partially infilled template and (*d*) mesostructured AgCl inverse opal [63]. Reproduced from Ref. [63] by permission of John Wiley & Sons Ltd. (**c**) The formation process of AgCl hollow cubes; (**d**) (*a*) XRD pattern, (*b–d*) FESEM, and (*e, f*) TEM images of AgCl hollow cubes [64]. (Reproduced from Ref. [64] by permission of the Royal Society of Chemistry)

agent (Fig. 13.9a, b). Detailedly, $AgNO_3$ was added into the prepared cubic NaCl suspension, along with the assistance of surfactant PVP to prevent the aggregation of AgCl particle. Ion exchange diffusion reaction between NaCl and Ag^+ in the solution led to the heterogeneous nucleation and continued growth of AgCl on the surface of the NaCl template. Finally, NaCl template would be removed by water washing and the AgCl cubic cages would be obtained. Similarly, AgCl nanoframe, AgBr cubic cage, and porous AgBr microsphere can also be synthesized via similar experimental steps [59–62].

3. *Other Methods*

Besides ion exchange method, there still exist other ways to prepare 3D AgX materials. For example, Braun et al. utilized AgCl–KCl eutectic system to prepare 3D mesoporous AgCl inverse opal [63]. As illustrated in Fig. 13.10a, AgCl–KCl eutectic powder was placed on the top of silica opal template. With increasing the temperature, the AgCl–KCl eutectic melted (eutectic temperature $= 318\ °C$) and flowed into the porous opal through a combination of capillary force and gravity, wetting the opal up to its top. The mesoporous AgCl inverse opal structure was obtained by dissolution of the silica colloidal template and KCl with 5% HF. As

shown in Fig. 13.10b-*a* and b-*c*, the AgCl–KCl eutectic infilled and solidified in colloidal crystal template. After removing template and KCl, a rather complex porous AgCl mesostructure containing features with characteristic dimensions of 100–200 nm is observed (Fig. 13.10b-*d*). Another feasible way to prepare 3D AgX material is one-pot growing method. Shen et al. synthesized a cuboidal AgCl hollow nanostructure by a simple one-pot reaction using $AgNO_3$ and CCl_4 as precursors (Fig. 13.10c) [64]. The key process in this strategy is dissolution–precipitation process. During this process, the Ag atoms in the core of the cubes gradually diffuse outward and react with CCl_4 on the surface, where Ag atoms could be oxidized by CCl_4 to form AgCl and deposited on the surface of each cube as a shell. In this case, Ag cations or atoms have a higher diffuse speed compared with the incoming Cl species, which causes a void space inside the cube and the formation of a hollow structure (Fig. 13.10d).

13.4.3 Facet Exposed

The crystal structure of AgX is a face-centered cubic belonging to the space group Fm3m. Hence, there exist several kinds of facet-exposed AgX crystal, such as hexahedron with {100}, octahedron with {111}, dodecahedron with {110}, tetrakaidecahedron with both {100} and {111}, trisoctahedron with {331}, icositetrahedron with {211} or {311}, tetrahexahedron with {210}, and hexoctahedron with {321} [25]. However, due to the higher surface energy of others facets, only {100} and {111} facets are usually stable on the crystal surface. Consequently, hexahedron, octahedron, and tetrakaidecahedron are the shapes of stable crystals (Fig. 13.11).
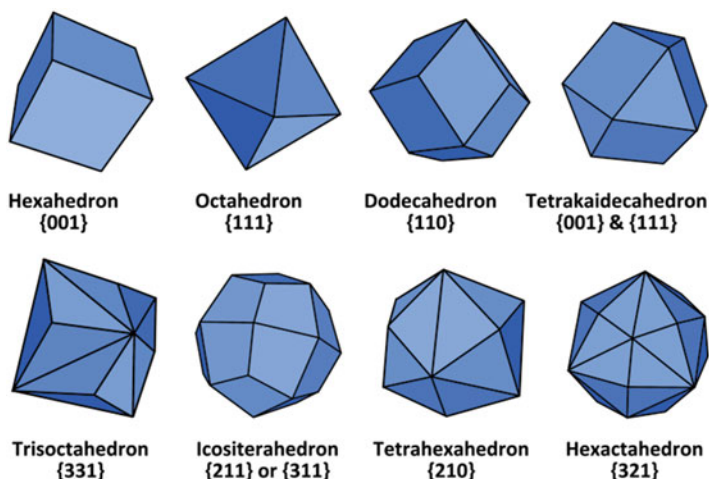

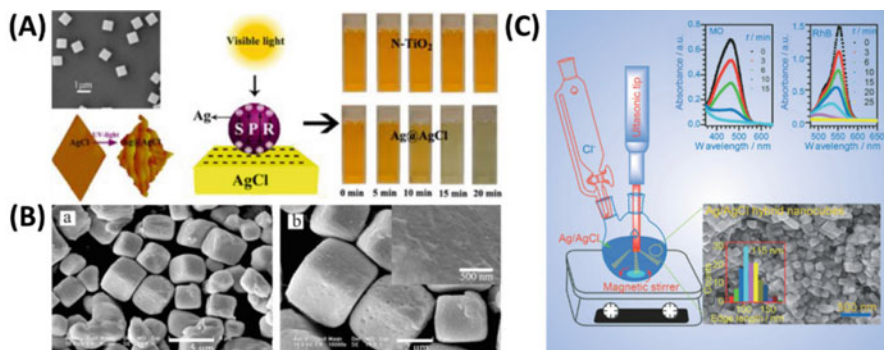**Fig. 13.11** Schematic diagram of different facet-exposed AgX crystal

Fig. 13.12 AgCl cube prepared by (**a**) precipitation method [41]. Reprinted with the permission from Ref. [41]. Copyright 2013 American Chemical Society. (**b**) Solvothermal method [70]. Reprinted from Ref. [70], Copyright 2011, with permission from Elsevier. (**c**) Sonochemical method [71]. (Reproduced from Ref. [71] by permission of John Wiley & Sons Ltd)

Normally, it is hard to control the morphology and exposed facets of AgX due to the high reaction rate between Ag^+ ions and X^- ions [65–71]. Therefore, it is necessary to slow down the reaction speed between Ag^+ ions and X^- ions to obtain AgBr crystals with regular morphology and specific exposed facets. By precisely controlling the injection speed of Ag^+ ions and X^- ions using the double-jet equipment, Tian et al. synthesized cubic AgCl and AgBr crystals with {100} exposed facets in the absence of structure-directing agents (Fig. 13.12a) [35, 36, 39–44]. The obtained cubic AgCl and AgBr photocatalytic exhibited excellent photocatalytic activity for organic contaminant degradation. Using methylene dichloride as chlorine source instead of inorganic chloride source, Dong et al. prepared cube Ag/AgCl via a hydrothermal method. In the hydrothermal process, the slow release of Cl^- ions is favorable to the formation of cubic Ag/AgCl morphology (Fig. 13.12b) [70]. Moreover, cubic AgCl can also be obtained with the assistance of structure-directing agents. For instance, Cho et al. [71] synthesized cube-shaped Ag/AgCl photocatalysts by a sonochemical route using PVP as the structure-directing agent (Fig. 13.12c). The obtained Ag/AgCl plasmonic photocatalysts show enhanced photocatalytic activity for the degradation of methyl orange (MO), Rhodamine B (RhB), and methylene blue (MB) under visible light irradiation.

Compared with {100} facet, the surface energy of {111} facet of AgX is a litter higher under common condition. So, the {111} facet easily disappears during the growth of AgX crystals. However, if the surface energy of {111} facet can be decreased to that of {100} facet by adding structure-directing agent, the {111} facet-exposed AgX crystals can be obtained. Enlightened by this principle, we synthesized different facet-exposed AgBr crystals by a double-jet precipitation method with the inherent Br^- as the structure-directing agent [36]. It was found that the morphology and exposed facets of the AgBr crystals were conveniently tailored by adjusting the concentration of Br^- ions, i.e., cubes (C-AgBr) with {100}
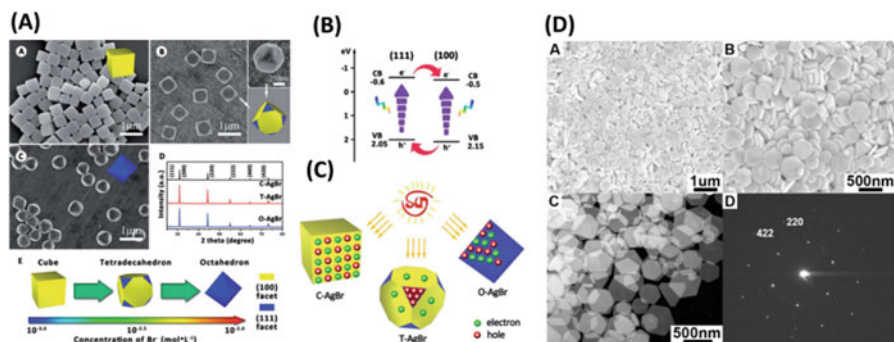
Fig. 13.13 (**a**) FE-SEM images and XRD patterns of different facet-exposed AgBr crystals and the illustration of morphology change as a function of Br^- ion concertation; (**b**) Band energy levels of {111} and {100} facets; (**c**) Illustration of the distribution of photo-generated electrons and holes on the different facet-exposed AgBr [36]. Reproduced from Ref. [36] by permission of the Royal Society of Chemistry. (**d**). SEM images, TEM image, and the corresponding SAED pattern of AgBr nanoplates [72]. (Reproduced from Ref. [72] by permission of the Royal Society of Chemistry)

facets, tetradecahedrons (T-AgBr) with both {100} and {111} facets, and octahe-drons (O-AgBr) with {111} facets were synthesized when the concentrations of Br^- ions were $10^{-3.0}$, $10^{-2.5}$, and $10^{-2.0}$ M, respectively (Fig. 13.13a). Br^- ions can clearly decrease the surface energies of the (100) and (111) surfaces, by which the growth rate of AgBr nuclei along the [100, 111] directions can be tuned by adjusting the concentration of Br^- ions, leading to the formation of AgBr crystals with different exposed facets. As shown in Fig. 13.13b, because the conduction band (CB) and valence band (VB) positions of the {111} facets are higher than those of the {100} facets, the {111} and {100} facets can form facet heterojunction struc-tures. Consequently, for the C-AgBr and O-AgBr which only have one kind of facet, the photo-generated electrons and holes will accumulate on the same facets, leading to a high recombination rate of electrons and holes. In the case of T-AgBr, the spatial isolation of photo-generated electrons and holes not only reduces the recombination rate but also effectively prevents the back reaction by isolating the reduction and oxidation reaction sites (Fig. 13.13c). Besides the inherent Br^- ion, organic chemicals, such as PVP and DMSO with –C=O and –S=O functional groups, can also play the role of structure-directing agent to lower the surface energy of {111} facet [72, 73] (Fig. 13.13d).

Although the facets with higher surface energy, such as {110}, {311}, and {15 5 2}, are thermodynamically unstable, they can still be prepared by adding special structure-directing agents. For example, Huang et al. synthesized AgBr microcrys-tals with different morphologies by ionic liquid (IL)-assisted hydrothermal method (Fig. 13.14a) [74]. In this method, four ionic liquids with different alkyl chains were used as the structure-directing agent. And the existence of ILs restricted step growth of AgBr {001} faces by restraining the diffusion of Ag^+, so the morphology of AgBr microcrystals could be tuned. With the assistant of 3-methylimidazolium bromides (C_4MimBr), AgBr dodecahedron crystals with exposed {110} facet were prepared.
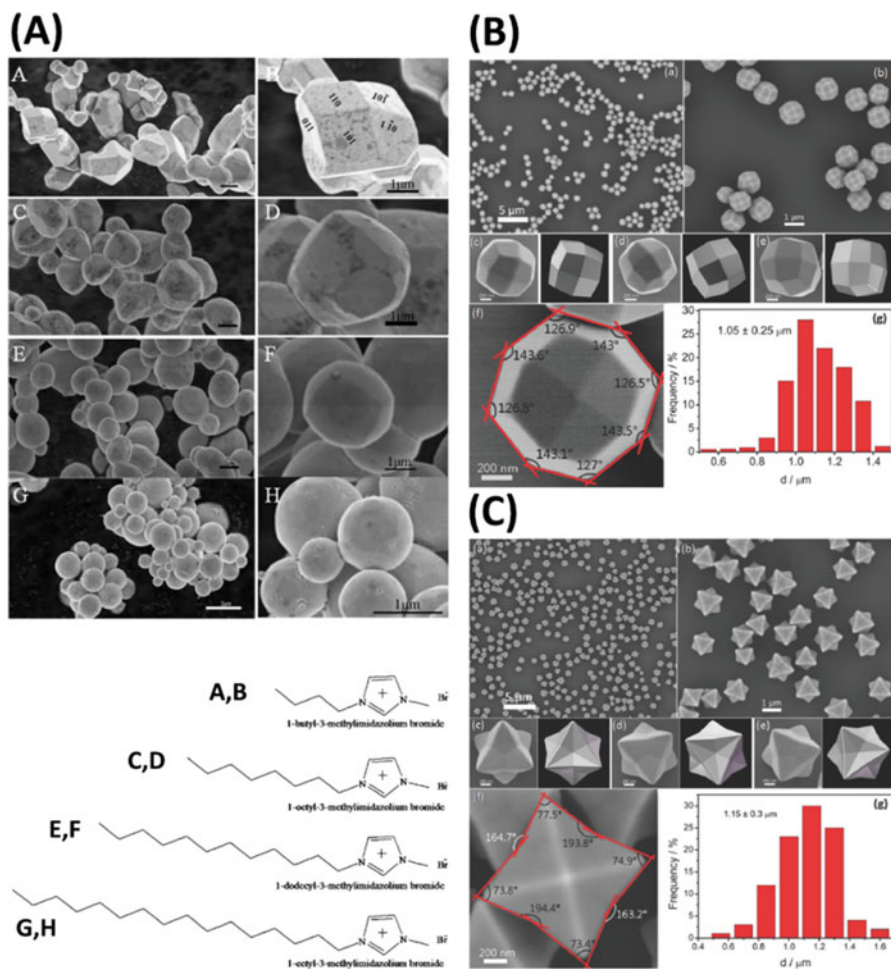
Fig. 13.14 (**a**) SEM images of samples synthesized with C$_4$MimBr, C$_8$MimBr, C$_{12}$MimB, and C$_{16}$MimBr, respectively [74]. Reproduced from Ref. [74] by permission of the Royal Society of Chemistry. (**b** and **c**). SEM images of AgCl crystals: (*a*) large-area and (*b*) enlarged. (*c*–*e*) in different orientations, with the corresponding geometrical models shown to the right of each SEM image. (*f*) A single AgCl crystal. (*g*) Size distribution of the as-prepared AgCl crystals [75]. (Reproduced from Ref. [75] by permission of the Royal Society of Chemistry)

Similarly, Zhang et al. found that exposed facets of AgCl crystals could be toiled from {311} to {15 5 2} using poly(diallyldimethylammonium) chloride (PDDA) as the both Cl source and structure-directing agent (Fig. 13.14b, c) [75].

13.5   Synthesis and Application of AgX-Based Heterojunction Structure

The most common heterojunction structure is based on a semiconductor-semiconductor architecture in which a p-type semiconductor usually closely contacts with an n-type semiconductor. This structure will result in a space charge region and an electric field at the interface, causing the directed flow of electrons to the CB of n-type semiconductor and holes to the VB of p-type semiconductor. This charge transfer can enhance the separating efficiency, charge carrier lifetime, and reaction rates [76–83]. Since AgX materials are prone to be reduced by the photo-generated electrons, combining with other semiconductor not only improves the separation rate of charge carriers but also promotes the photostability of AgX materials. Based on the structure, the AgX-based heterojunction structures can be classified into two types: AgX-Y and Ag-AgX-Y (Y is another semiconductor).

13.5.1   AgX–Y

AgX-Y is composed of AgX and another semiconductor Y. The closely contacting interface between AgX and Y can be produced via ion exchange method. For example, Huang et al. fabricated AgI–BiOI hierarchical hybrids by ion exchange between BiOI hierarchical microspheres and $AgNO_3$ (Fig. 13.15a) [77]. It was found that AgI nanoparticles were uniformly anchored on the surface of BiOI nanosheets and the particle size of AgI can be toiled from 55–16 nm by the addition of poly (vinylpyrrolidone) surfactant molecules. Besides ion exchange method, adsorption of organics with halogen or $Ag(NH_3)_2^+$ beforehand can also create the close contact between AgX and semiconductor Y. For instance, $[C_{16}min]Br$ ionic liquid was used to adsorb on the surface of BiPO4 to form $AgBr/BiPO_4$ heterojunction structure [83]. Beneficial from the close contact, the photo-generated charges can be efficiently separated, as shown in Fig. 13.15b, c. Some of the synthesized AgX–Y photocatalysts are summarized in Table 13.2.

13.5.2   Ag–AgX–Y

Compared to AgX–Y, Ag–AgX–Y can more effectively absorb visible light by the surface plasmon resonance effect (SPR) of Ag nanoparticles formed on the surface of AgX. Therefore, Ag–AgX–Y not only can respond to visible light but also has higher electron–hole separation rate. According to the substrates (Y), Ag–AgX–Y can be classified into several classes as follows.
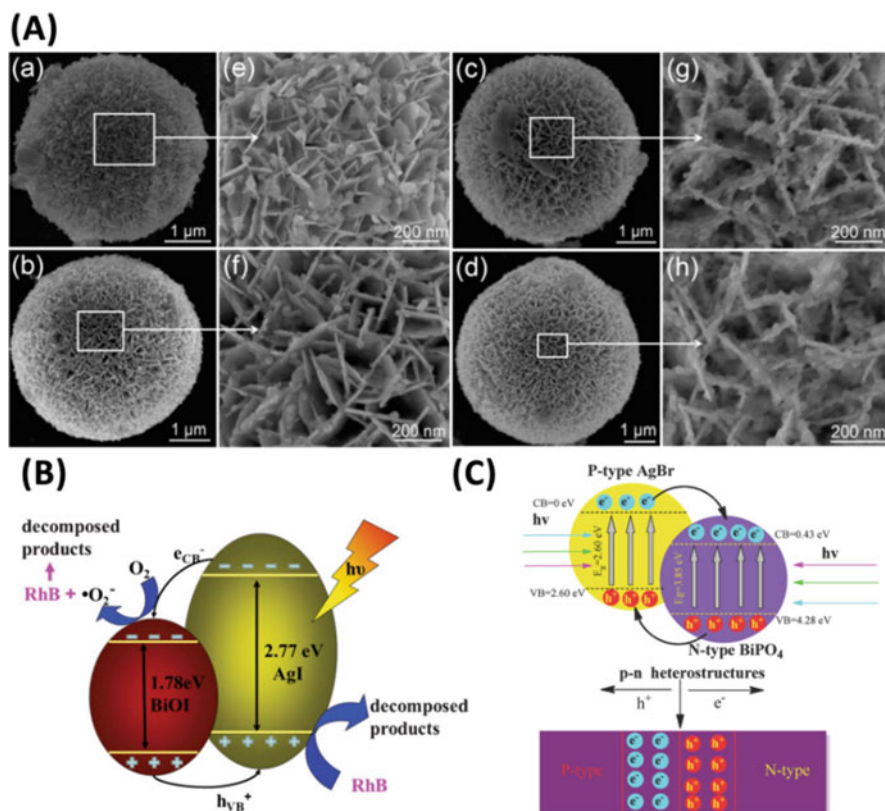
Fig. 13.15 (**a**) SEM images of AgI–BiOI with different sized AgI (55 nm, 36 nm, 24 nm, and 16 nm) [77]. Reproduced from Ref. [77] by permission of the Royal Society of Chemistry. (**b** and **c**) Photocatalytic mechanism of (**b**) AgI–BiOI [77] and (**c**) AgBr-BiPO$_4$ [83]. (Reproduced from Ref. [83] by permission of the Royal Society of Chemistry)

Table 13.2 Different heterojunction structure of AgX–Y

Name	Application	References
AgI–BiOI	Photodegrading 2,4-dichlorophenol	[77]
AgI–BiOI	Photodegrading RhB	[78]
AgI–TiO$_2$	Photodegrading RhB	[79]
AgI–N–TiO$_2$	Photodegrading MO	[80]
AgBr–ZnO	Photodegrading RhB	[81]
AgBr–BiWO$_6$	Photodegrading MB	[82]
AgBr–BiPO$_4$	Photodegrading MB	[83]

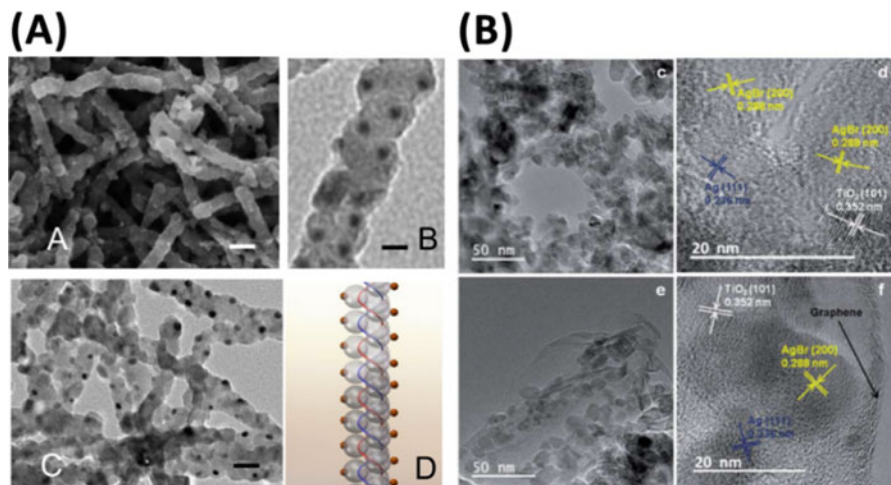**Fig. 13.16** (**a**) SEM and TEM images of Ag–AgCl–TiO$_2$ [84]. Reprinted from Ref. [84], Copyright 2015, with permission from Elsevier. (**b**) TEM images of Ag–AgBr–TiO$_2$–GO [87]. (Reproduced from Ref. [87] by permission of the Royal Society of Chemistry)

13.5.2.1 Ag–AgX–TiO$_2$

Titanium dioxide (TiO$_2$) has been widely researched as a kind of traditional photocatalytic material with the advantages of low cost and high stability. Generally, Ag–AgX–TiO$_2$ is synthesized by cation surfactant adsorption and photoreduction technique [84–88]. In detail, a layer of cetyltrimethylammonium chloride (CTAC) or cetyltrimethylammonium bromide (CTAB) is absorbed on the surface of TiO$_2$. Subsequently, Ag$^+$ ions are added and react with halogen ions on the surface of TiO$_2$ to form AgX nanoparticles. Following this synthesis strategy, Ag-AgCl-TiO$_2$ and Ag-AgBr-TiO$_2$ were prepared in Fig. 13.16a, b. And thanks to the heterojunction structure, the photocatalytic activity and charge separation ability had been improved greatly [84, 87].

For the establishment of core–shell structure, its main aim is to improve the stability of AgX. Although the Ag nanoparticle can capture photo-generated electrons to prevent AgX been photo-corroded, the chemicals in the reaction system can also destroy AgX and decrease its photocatalytic activity. Therefore, it is a feasible and effective way to prevent the deterioration of stability by covering with a layer of stable semiconductor. Besides with good carriers transfer ability, this layer of semiconductor must be thin enough to transmit visible light. Moreover, it also needs to be porous for the transfer of reactants and products. Taking the above requirements into consideration, TiO$_2$ is a good choice.

As shown in Fig. 13.17a, we successfully coated TiO$_2$ shell layer on the cubic AgCl crystals by a gradual temperature rise process [35]. During this process, the pH value of suspension and temperature rise rate are the key steps, which can effectively control the hydrolysis rate of Ti(SO$_4$)$_2$, or else a mass of TiO$_2$ would aggregate
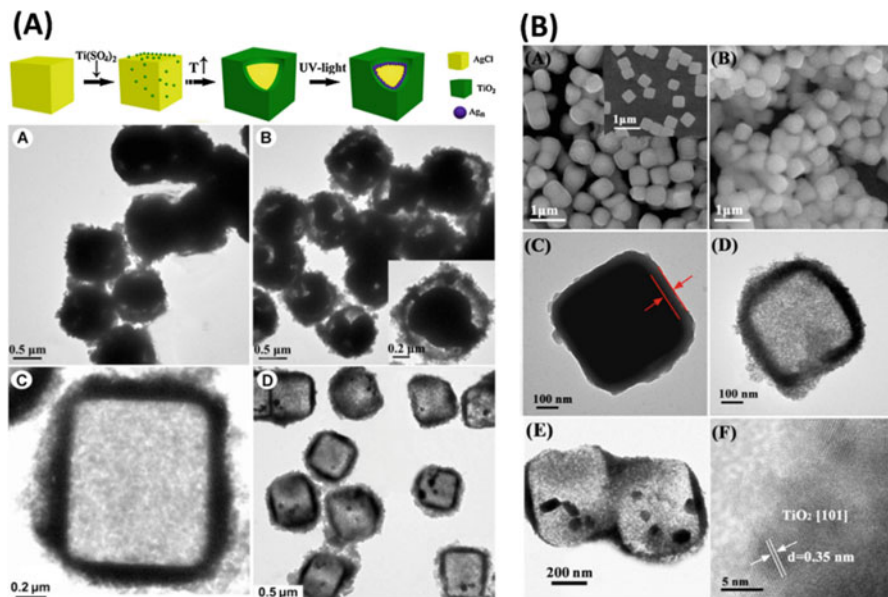
Fig. 13.17 (**a**) Synthetic route of the sandwich-structured AgCl@Ag@TiO$_2$ plasmonic photocatalyst and TEM images of AgCl@TiO$_2$ bombed by electron beams for (*A*) 2 min and (*B*) 10 min. TEM images of (*C*) AgCl@TiO$_2$ and (*D*) AgCl@Ag@TiO$_2$ treated with Na$_2$S$_2$O$_3$ solution [35]. Reprinted from Ref. [35], Copyright 2014, with permission from Elsevier. (**b**) SEM images of AgBr@TiO$_2$ before (*A*) and after (*B*) hydrothermal treatment. TEM image of AgBr@TiO$_2$ (*C*), TiO$_2$ shell (*D*) and Ag@TiO$_2$ shell. High-resolution TEM image of AgBr@Ag@TiO$_2$ [44]. (Reprinted from Ref. [44], Copyright 2016, with permission from Elsevier)

together. In Fig. 13.17a*A–D*, it could be found that the thickness of TiO$_2$ shell layer is about 100 nm. Moreover, after being etched by Na$_2$S$_2$O$_3$ solution, there exist several Ag nanoparticles inside the TiO$_2$ shell, which is the evidence for the fully coating of TiO$_2$ shell. In addition, our group also reported the synthesis of AgBr@–Ag–TiO$_2$ with core–shell structure, in Fig. 13.17b [44]. In this work, a series of AgBr@Ag–TiO$_2$ with different shell thickness (0.01, 0.02, 0.03 and 0.05 μm) has been prepared by similar method, and the addition of NH$_3$H$_2$O is found as a key factor to control the thickness of TiO$_2$ shell layer.

13.5.2.2 Ag–AgX–C$_3$N$_4$

Recently, carbon nitride (C$_3$N$_4$) has received much attention as a stable, metal-free, and visible light-driven photocatalyst [89–94]. Commonly, the C$_3$N$_4$ nanosheets are delaminated from the bulk C$_3$N$_4$ by HCl solution. This acid treatment process can increase the abundance of amino functional groups on the surface of the C$_3$N$_4$ nanosheets. Furthermore, the amino groups with the lone pairs of electrons on the N atom in the tri-s-triazine ring structure can bind strongly to Ag$^+$. Therefore, as
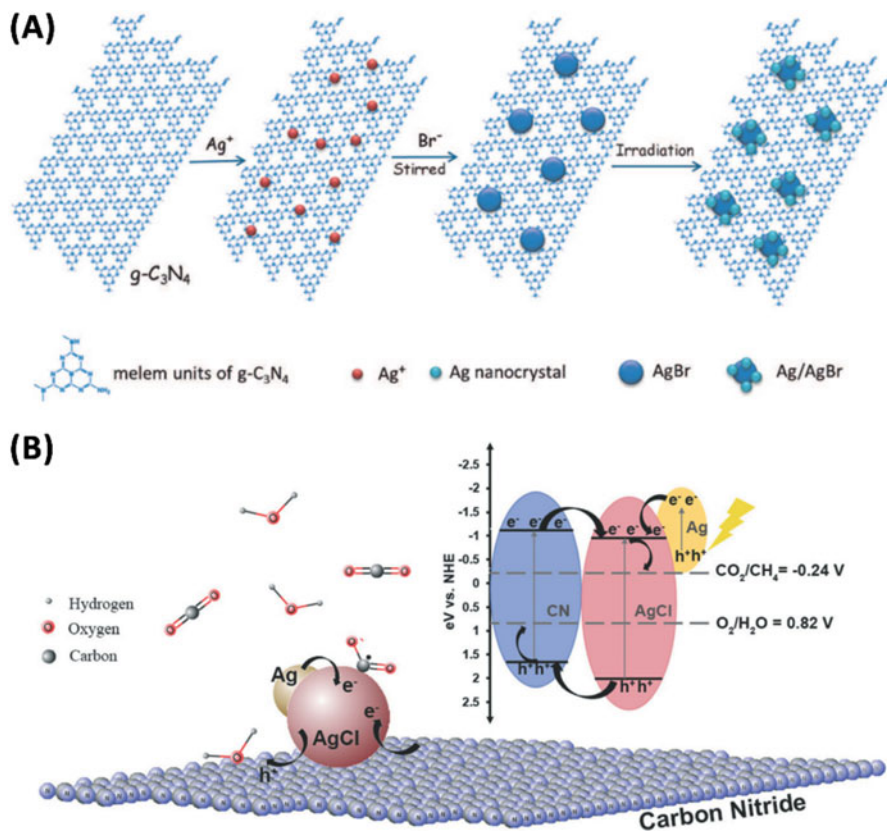
Fig. 13.18 (**a**) Schematic representation of Ag–AgBr–C$_3$N$_4$ nanocomposites [89]. Reproduced from Ref. [89] by permission of John Wiley & Sons Ltd. (**b**) Photocatalytic mechanism of Ag-AgCl-C$_3$N$_4$ [90]. (Reproduced from Ref. [90] by permission of the Royal Society of Chemistry)

shown in Fig. 13.18a, during the synthesis of Ag–AgX–C$_3$N$_4$, Ag$^+$ is added into suspension and adsorbed on the surface of C$_3$N$_4$ nanosheets beforehand. Subsequently, the added X$^-$ will react with the Ag$^+$ in situ to form AgX nanoparticles. For example, Zhang et al. prepared Ag-AgBr-C$_3$N$_4$ by this method and this photocatalytic material exhibited 28-fold and sixfold enhancements in photodegrading RhB than bare C$_3$N$_4$ and Ag–AgBr nanoparticles [89]. Chai et al. reported that the amount of AgCl in Ag–AgCl–C$_3$N$_4$ can be adjusted with the different addition of AgNO$_3$ [90]. Generally, the CB of C$_3$N$_4$ is more negative than CB of AgX, so that the photo-generated electrons will transfer from C$_3$N$_4$ to AgX and finally be trapped by the Ag nanoparticles on the surface of AgX due to the lower Fermi level. And the photo-generated holes will transfer to C$_3$N$_4$ and take participate in the degrading reactions (Fig. 13.18b).
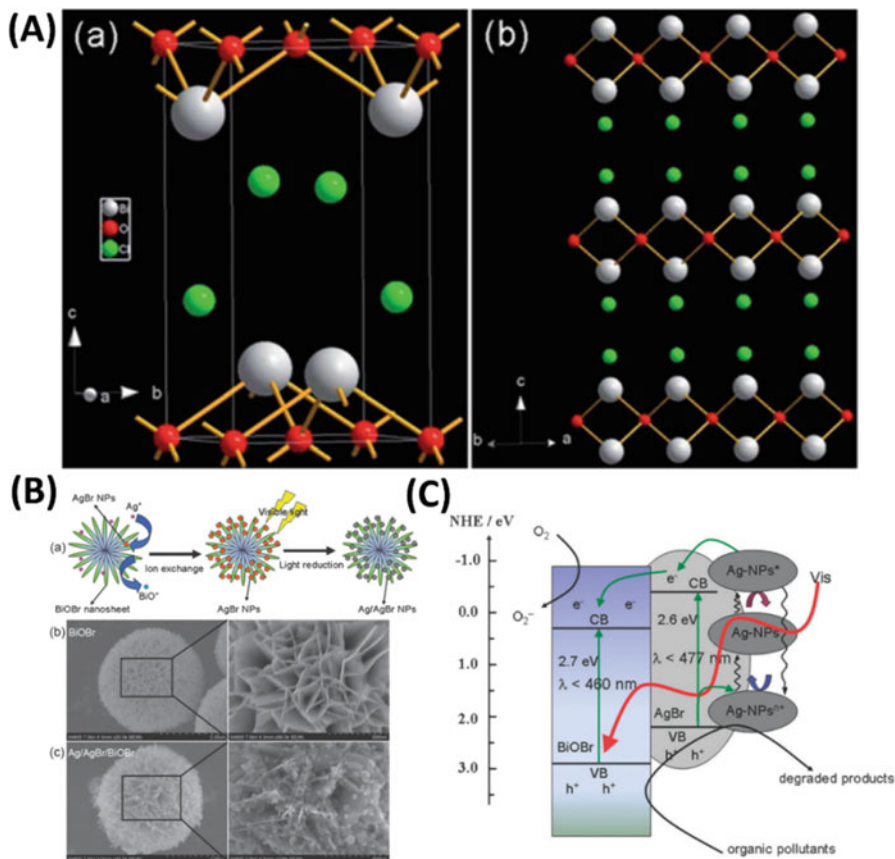
Fig. 13.19 (**a**) Schematic diagram of (*a*) unit cell and (*b*) crystal structure of BiOCl. (**b**) Synthetic route of Ag/AgBr/BiOBr hybrid and SEM images of BiOBr and Ag/AgBr/BiOBr hybrid; (**c**) photocatalytic reaction mechanism of the Ag/AgBr/BiOBr hybrid [98]. (Reproduced from Ref. [98] by permission of the Royal Society of Chemistry)

13.5.2.3 Ag–AgX–BiOX

Bismuth oxyhalides BiOX (X = Cl, Br, I) have been paid close attention for their outstanding optical and photocatalytic properties [95–97]. From the literatures, we know that all BiOX crystal is ascribed to tetragonal matlockite structure. Taking BiOCl as an example, BiOX are characterized by the layered structure that are composed of [Bi_2O_2] slabs interleaved with double halogen atom slabs along the [001] direction (Fig. 13.19a) [98]. Utilizing this structured characteristic, Huang et al. synthesized a series of AgX–BiOX (AgBr–BiOBr and AgI–BiOI) via ion exchange method [99, 100]. In this process, flowerlike BiOX particles were prepared firstly. Then, through the ion exchange reaction between BiOX and Ag^+ in ethylene glycol, AgX nanoparticles deposited on the surface of BiOX nanosheets with high

dispersity, while the produced BiO^+ ions would dissolve in the solvent ($BiOBr + Ag^+$ = $AgBr + BiO^+$) (Fig. 13.19b). By this process, the AgX would be in situ formed on the surface of BiOX. This intimate connection between BiOX and AgX is beneficial to the transfer of photo-generated carriers (Fig. 13.19c). Besides this method, AgX–BiOX can also be obtained via the direct reaction of Bi^{3+}, Ag^+ and X^- in the hydrothermal process [101–103].

13.5.2.4   Ag–AgX–AgY

Similar to AgX, the other Ag salts (Ag–AgX–AgY), such as Ag_3PO_4, Ag_2O, Ag_2CO_3, $AgVO_3$, etc., are also visible light-driven photocatalysts with high photocatalytic activity. Combining with these Ag salts to construct heterojunction can greatly improve the photocatalytic performance of AgX [104–107]. As we all know, the solubility product (Ksp) of AgX is much lower than the most of other Ag salts. Consequently, it is feasible to construct the heterojunction of AgX–AgY by the means of ion exchange method. For example, Wu et al. utilized NaBr solution to exchange the PO_4^{3+} ions in Ag_3PO_4 to form $AgBr–AgPO_4$ (Fig. 13.20a). In addition, $Ag–AgCl–Ag_2O$ [105], $Ag–AgBr–AgVO_3$ [106], and $Ag–AgBr–Ag_2CO_3$ [107] can also be prepared by this ion exchange method (Fig. 13.20b, c). Being benefited from this heterojunction, photo-generated carriers can be effectively separated (Fig. 13.20d).

13.6   Z-Scheme Structure

Constructing Z-scheme structure is another effective way to promote the separation rate of photo-generated carriers. Moreover, beneficial from the special transfer process of electrons and holes, the higher redox ability of photocatalytic composites can be reserved via Z-scheme structure [108–113]. In Z-scheme structured AgX-Ag-Y photocatalytic material, the semiconductor Y has the same metallic element with AgX, which can facilely be in situ generated via photo-reduction process. The in situ formed Ag nanoparticles can be stably anchored on the surface of AgX inhibiting the exfoliation of Ag nanoparticles from AgX surface [111]. Moreover, the tight solid-solid contact interface between Ag nanoparticles and AgX can reduce the electric resistance, beneficial to forming Ohmic contact. Interestingly, different from the conventional Z-scheme structure, the role of Ag nanoparticles, electron mediator or photosensitizer, is determined by the energy band structure of AgX and semiconductor Y. According to the energy levels of the two semiconductors, the visible light-driven Z-scheme AgX–Ag–Y can be classified into three types, as shown in Fig. 13.21.
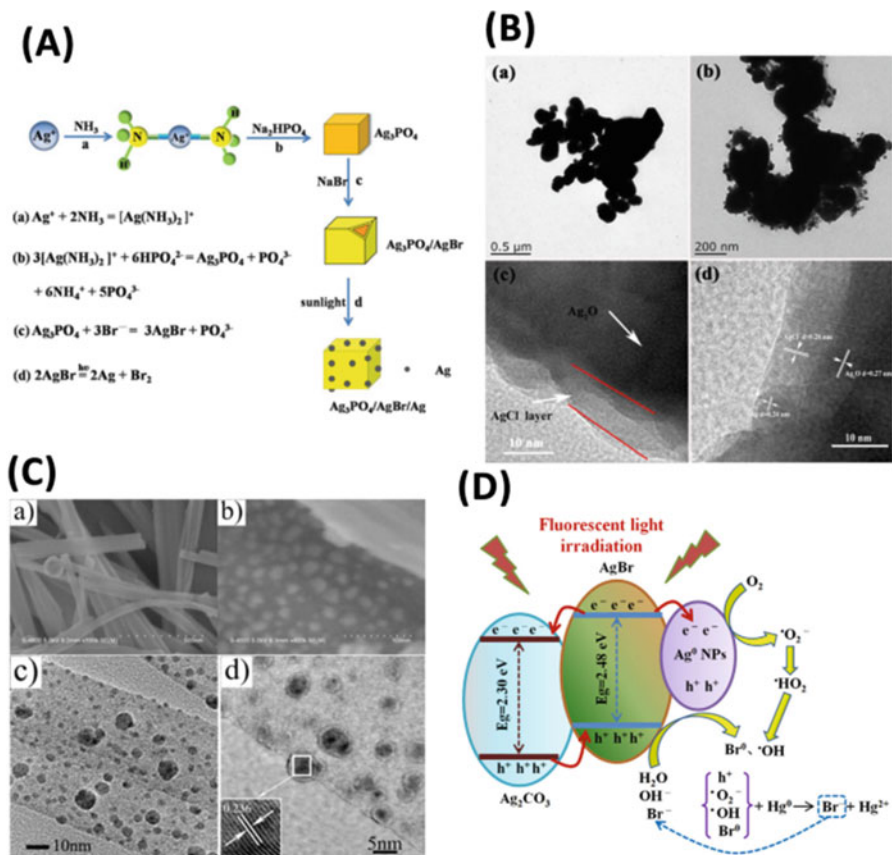
Fig. 13.20 (**a**) Schematic illustration of the growth process of Ag–AgBr–AgPO$_4$ [104]. Reproduced from Ref. [104] by permission of the Royal Society of Chemistry. (**b**) TEM images of Ag–AgCl–Ag$_2$O [105]. Reprinted from Ref. [105], Copyright 2017, with permission from Elsevier. (**c**) SEM and TEM images of Ag–AgBr–AgVO$_3$ [106]. Reprinted from Ref. [106], Copyright 2014, with permission from Elsevier. (**d**) photocatalytic mechanism and charge transfer in Ag–AgBr–Ag$_2$CO$_3$ [107]. (Reprinted with the permission from Ref. [107]. Copyright 2016 American Chemical Society)

1. *Type A*

In type A, the Z-scheme AgX-Ag-Y photocatalytic material is composed of AgCl ($E_g = 3.2$ eV) and another semiconductor Y with narrower band gap ($E_g < 3.0$ eV). As a result, under visible light irradiation, semiconductor Y can adsorb photons and generate electron–hole pairs, while AgCl cannot. Furthermore, to meet the requirement of Z-scheme structure, the CB of semiconductor Y should be lower than that of AgCl ($E_{CB, AgCl} = -0.05$ eV). In this case, the Ag nanoparticles simultaneously serve as the electron mediator and photosensitizer, differing from the role of noble metal nanoparticles in common Z-scheme structured photocatalytic materials.

As illustrated in Fig. 13.21, Ag nanoparticles can produce photo-generated electrons and holes via SPR effect under visible light irradiation. Due to the store
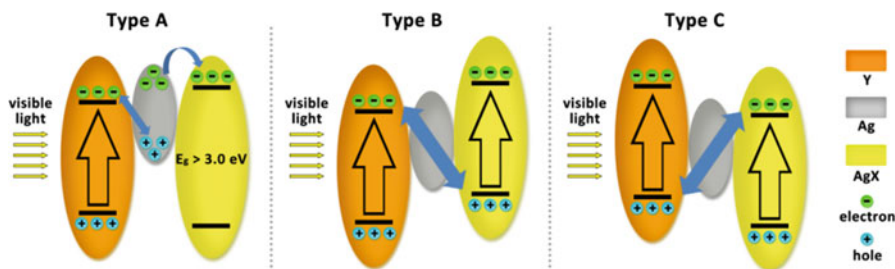
Fig. 13.21 Schematic of the three types of Z-scheme structured AgX-Ag-Y photocatalytic materials
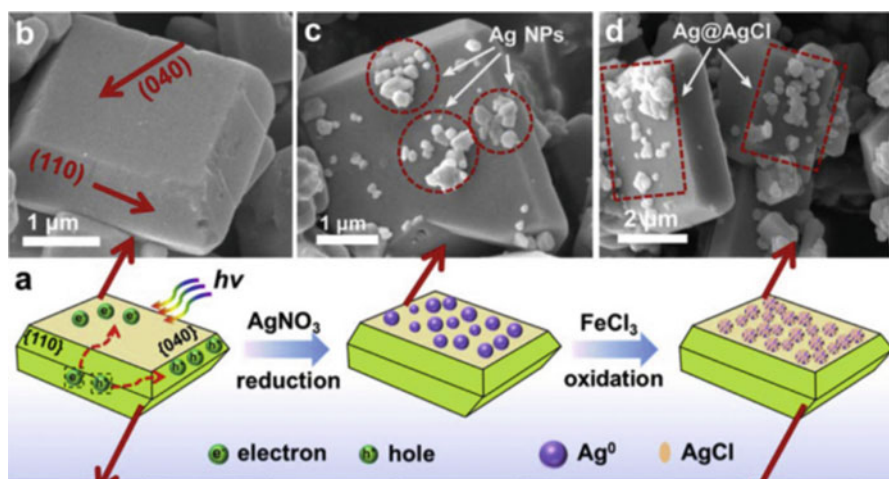

Fig. 13.22 (**a**) Schematic illustration of the formation process of the Ag@AgCl/BiVO$_4$ heterojunction photocatalyst. SEM images of the as-prepared BiVO$_4$ (**b**), Ag/BiVO$_4$ (**c**), and Ag@AgCl/BiVO$_4$ (**d** and **e**) [114]. (Reprinted from Ref. [114], Copyright 2015, with permission from Elsevier)

of electrons in the lowest unoccupied orbital of Ag, the Fermi energy level of Ag nanoparticle will be lifted. Afterward, the superfluous electrons will migrate into the CB of the neighboring AgCl. Simultaneously, the photo-generated electrons in CB of semiconductor Y will transfer to Ag nanoparticle and combine with the holes in the highest occupied orbital of Ag, while the photo-generated holes in VB of semiconductor Y can participate in the photocatalytic reaction. Beneficial from this special mechanism for separating photo-generated carriers, Z-scheme structured AgX-Ag-Y photocatalytic material exhibit superior photocatalytic activity for organic compound degradation [114–122]. For example, Wu et al. designed a hierarchical Z-scheme photocatalyst Ag@AgCl/BiVO$_4$ (Fig. 13.22) [114]. In this system, the metallic Ag species not only act as the solid-state electron mediator but also absorb the photons by SPR effect. Compared with pristine BiVO$_4$, the

photocatalytic performance for degrading RhB was enhanced about 300 times. Moreover, Yu et al. prepared $H_2WO_4 \cdot H_2O/Ag/AgCl$ composite nanoplates by a one-step ionic reaction between $Ag_8W_4O_{16}/Ag$ nanorods and HCl aqueous solution [119]. The photocatalytic experiments indicated that the $H_2WO_4 \cdot H_2O/Ag/AgCl$ composite nanoplates exhibited a much higher photocatalytic activity than the one-component ($H_2WO_4 \cdot H_2O$) or two-component (such as Ag/AgCl and $H_2WO_4 \cdot H_2O/Ag$) photocatalysts.

2. Type B

For type B photocatalytic material, the Z-scheme AgX-Ag-Y is composed of AgX (X = Br or I) and another semiconductor Y with narrower band gap ($E_g < 3.0$ eV). Moreover, both the CB and VB energy levels of semiconductor Y are lower than those of AgBr ($E_{CB\text{-}AgBr} = -0.3$ eV, $E_{VB\text{-}AgBr} = 2.3$ eV) or AgI ($E_{CB\text{-}AgI} = -0.4$ eV, $E_{VB\text{-}AgBr} = 2.36$ eV). Therefore, the electrons in the VB of AgX and semiconductor Y can be excited to the corresponding CB under visible light illumination. The photo-generated electrons in the CB of semiconductor Y can migrate into Ag nanoparticles. Simultaneously, the photo-generated holes in VB of AgX will flow into Ag nanoparticles easily and recombine with the photo-generated electrons from semiconductor Y. Beneficial from the above carriers transfer process, the photo-generated electrons with stronger reduction power in CB of AgX and photo-generated holes with higher oxidation ability in VB of semiconductor Y can be reserved. This advantage will lead to higher photocatalytic activity of Z-scheme structured AgX based photocatalysts [37, 101, 123–129]. For instance, Fan et al. synthesized $Ag/AgBr/AgIn(MoO_4)_2$ nanosheets by in situ photoreduction of $AgBr/AgIn(MoO_4)_2$ composites (Fig. 13.23a) [123]. It was found that $Ag/AgBr/AgIn(MoO_4)_2$ composites exhibited dramatic enhanced photocatalytic activity for tetracycline degradation when compared with $AgIn(MoO_4)_2$ nanosheets, Ag/AgBr nanoparticles and $Ag/AgIn(MoO_4)_2$ composites. Yang et al. reported a facile in
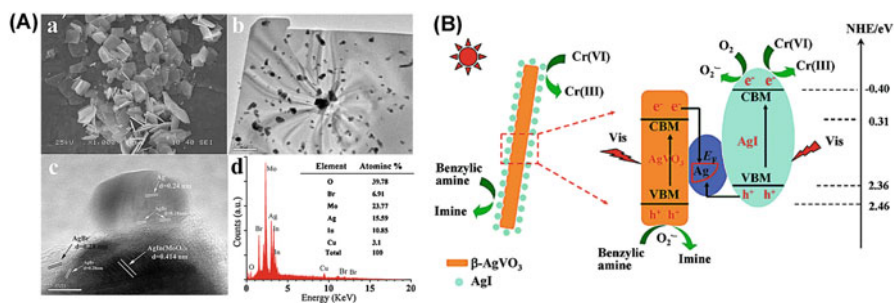
Fig. 13.23 (**a**) (*a*) FESEM image of $AgIn(MoO_4)_2$ nanosheets. (*b–d*) TEM, HRTEM, EDX of $Ag/AgBr/AgIn(MoO_4)_2$ [123]. Reprinted from Ref. [123], Copyright 2015, with permission from Elsevier. (**b**) Photocatalytic mechanism of $AgI/AgVO_3$ toward the selective oxidation of benzylic amine and reduction of Cr(VI) under visible light irradiation [124]. (Reproduced from Ref. [124] by permission of the Royal Society of Chemistry)
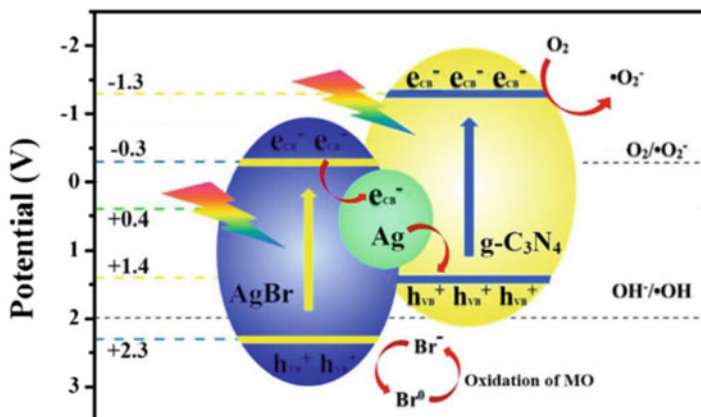
Fig. 13.24 Generation, separation and transportation of h_{VB}^+ and e_{CB}^- at the interface of the visible light-driven Ag@AgBr/g-C$_3$N$_4$ plasmonic photocatalyst [130]. (Reprinted from Ref. [130], Copyright 2014, with permission from Elsevier)

situ ion exchange approach to prepared AgI/AgVO$_3$ nanocomposites with β-AgVO$_3$ nanoribbons as the Ag source and support to immobilize AgI (Fig. 13.23b) [124]. The as-prepared composites can serve as highly efficient visible light-driven photocatalysts toward selective oxidation of benzylic amine to imine and reduction of toxic Cr (VI) ions. It also found that the considerable improvement in the photocatalytic redox properties of AgI/AgVO$_3$ is mainly ascribed to the efficient separation of photoinduced electrons/holes via a Z-scheme bridge mechanism of formed Ag/AgI/AgVO$_3$, in which Ag nanoparticles serve as the charge migration bridge.

3. *Type C*

Similar to Type B, the Z-scheme structured AgX-Ag-Y photocatalytic material in Type C is also composed of AgX and semiconductor Y, in which both of them can absorb visible light. However, as shown in Fig. 13.21c, the CB and VB of semiconductor Y is higher than that of AgX. Consequently, after the recombination process, the photo-generated electrons with higher reduction ability in CB of semiconductor Y and holes with better oxidation property in VB of AgX will be reserved. For example, in the system of AgBr–Ag–C$_3$N$_4$, photo-generated carriers are efficiently separated via Z-scheme structure Fig. 13.24) [93, 130]. Afterward, the electrons in CB of C$_3$N$_4$ will further react with O$_2$ to form. O$_2^-$ radicals and holes in VB of AgBr will generate Br^0 to oxide organic contaminants.

13.7 Recoverable AgX Photocatalytic Materials

The key problem that restrains the application of nano- or micro-sized AgX-based photocatalytic materials in waste water treatment is how to effectively separate and recycle the used photocatalysts. Traditional centrifugation and filtration strategy will not merely cause serious loss of photocatalysts but high energy consumption [131]. In the past 10 years, two strategies were introduced to improve the recoverability of AgX-based photocatalytic materials. One is loading the photocatalysts on the substrates, and another is combining with magnetic components.

13.7.1 Loaded on the Substrates

Although conventional 2D substrates for loading photocatalysts, such as ITO glass and metal foil, can be conveniently recycled, they suffer from the disadvantage of low surface area. Thus, recently, a series of substrates with high surface area (Al_2O_3 mesoporous microsphere, 3D graphene aerogels, and nylon mesh) were utilized to load AgX. For instance, He et al. immobilized the plasmonic Ag–AgI with photo-induced self-stability on mesoporous Al_2O_3 by a wet impregnation–precipitation and in situ photoreduction method [132]. Niu et al. synthesized a novel 3D structure AgX/GA (X = Br, Cl) composites with a macroscopic block appearance (Fig. 13.25a). Owing to the unique structure, this bulk composite material could just be recycled by directly clipping out using tweezers and washed with deionized water several times [133]. Tian et al. successfully fabricated Ag@AgBr gelatin film by embedding Ag@AgBr particles into a gelatin matrix and constructing 3D network structures via the cross-linking reaction between gelatin and cross-linking agent 1,3-bis(vinylsulfonyl) propanol, in Fig. 13.25b–e [40]. Beneficial from the SPR effect of Ag and excellent penetrability of 3D network structure for reactants
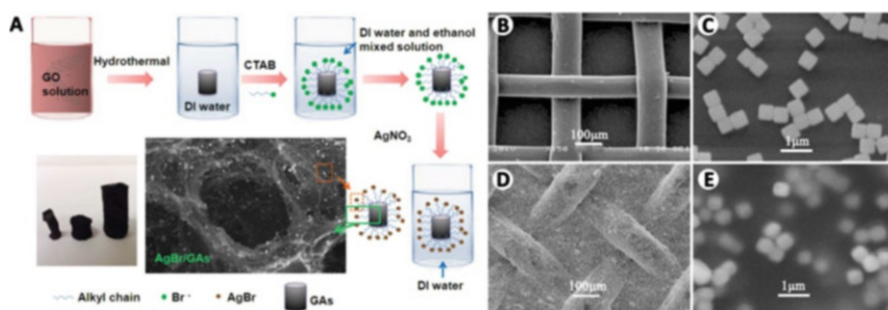

Fig. 13.25 (**a**) Fabrication of the AgBr/gas 3D photocatalytic composite materials [133]. Reproduced from Ref. [133] by permission of John Wiley & Sons Ltd. SEM images of (**b**) nylon mesh; (**c**) Ag@AgBr grains, (**d**) and (**e**) Ag@AgBr-gelatin film loaded on nylon mesh [40]. (Reprinted from Ref. [40], with kind permission from Springer Science+Business Media)

and products, Ag@AgBr-gelatin film showed excellent visible light activity for MO degradation. Based on recycle experiments, the film exhibited excellent stability and recyclability in the application of organic contaminant degradation. Moreover, it should be noticed that this synthetic route can be used to fabricate photocatalytic films in a large scale, which is meaningful for practical application.

13.7.2   Combined with Magnetic Components

Besides loading AgX materials on subtracts, immobilizing photocatalysts on the surface of magnetic nano- or microparticles is another effective strategy to enhance the recoverability, by which the photocatalysts can be easily separated by an external magnet under the premise of keeping photocatalytic activity. Recently, $CoFe_2O_4$ [134–136], Fe_3O_4 [137–139], Fe_2O_3 [140–142], and γ-Fe_2O_3 [131] were used as photocatalyst carriers to obtain efficient recyclable AgX-based materials for water treatment. For example, Xu et al. attempted to construct ferromagnetic plasmonic nanophotocatalysts by coupling Ag/AgCl with magnetic material $CoFe_2O_4$, which enhanced the photo-activity of Ag/AgCl/$CoFe_2O_4$ [134]. They also prepared Ag/AgBr@Fe_2O_3 magnetic photocatalyst by solvothermal process. The Ag/AgBr was covered by Fe_2O_3 and formed a uniquely core–shell nanostructure, which would provide a high surface area and numerous active sites for the photocatalytic reaction (Fig. 13.26a) [140]. Zhang et al. reported a magnetic adsorptive photocatalyst composite, Ag/AgCl-magnetic activated carbon (MAC) synthesized via a facile deposition–precipitation–photoreduction method (Fig. 13.26b) [143]. The resulting composites possessed quasi-superparamagnetic behavior and exhibited good visible light-induced photocatalytic activity toward the inactivation of *E. coli* K-12 and degradation of methyl orange and phenol.

   Although these composite photocatalysts can be successfully separated by applying an external magnetic field, there still exist some deficiencies, such as wide size distribution and irregular morphological structures. These deficiencies will cause a longer time for completely harvesting photocatalysts. To solve this problem, Tian et al. fabricated core–shell structured γ-Fe_2O_3@SiO_2@AgBr:Ag composite microspheres with narrow size distribution by a versatile multistep route, including solvothermal method to fabricate magnetic core, modified Stöber method to coat SiO_2 interlayer, electrostatic assembly to deposit AgBr shell, and light reduction to form Ag nanoparticles (Fig. 13.26c, d) [131]. Beneficial from the narrow size distribution, high saturation magnetization, and superparamagnetic property, the core–shell structured γ-Fe_2O_3@SiO_2@AgBr:Ag shows excellent magnetic separation and recovery performances (completely harvesting in 30 s), as shown in Fig. 13.26e.
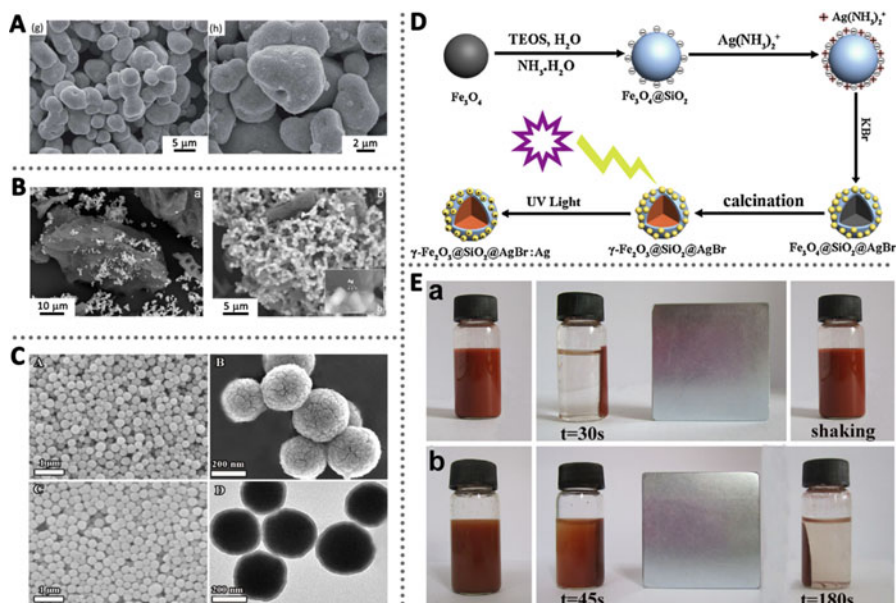
Fig. 13.26 SEM images of (**a**) 5% Ag/AgBr@Fe₂O₃ [140]. Reproduced from Ref. [140] by permission of the Royal Society of Chemistry. (**b**) Ag/AgCl-AC and Ag/AgCl-MAC [143]. Reprinted from Ref. [143], Copyright 2014, with permission from Elsevier. (**c**) Fe₃O₄ and γ-Fe₂O₃@SiO₂@AgBr:Ag [131]. (**d**) Schematic diagram illustrating the synthetic route of core–shell structured γ-Fe₂O₃@SiO₂@AgBr:Ag composite; (**e**) magnetic separation tests for γ-Fe₂O₃@SiO₂@AgBr:Ag and Fe₃O₄@SiO₂@AgBr:Ag using a cubic Nd-Fe-B magnet [131]. (Reprinted from Ref. [131], Copyright 2014, with permission from Elsevier)

References

1. Qiu B-C, Zhu Q-H, Xing M-Y, Zhang J-L (2017) A robust and efficient catalyst of $Cd_xZn_{1-x}Se$ motivated by CoP for photocatalytic hydrogen evolution under sunlight irradiation. Chem Commun 53:897–900

2. Qiu B-C, Zhu Q-H, Du M-M, Fan L-G, Xing M-Y, Zhang J-L (2017) Efficient solar light harvesting CdS/Co₉S₈ hollow cubes for Z-scheme photocatalytic water splitting. Angew Chem 129:2728–2732

3. Wu Q-F, Bao S-Y, Tian B-Z, Xiao Y-F, Zhang J-L (2016) Double-diffusion-based synthesis of BiVO₄ mesoporous single crystals with enhanced photocatalytic activity for oxygen evolution. Chem Commun 52:7478–7481

4. Xing M-Y, Zhang J-L, Chen F, Tian B-Z (2011) An economic method to prepare vacuum activated photocatalysts with high photo-activities and photosensitivities. Chem Commun 47:4947–4949

5. Du J, Du Z-L, Hu J-S, Pan Z-X, Shen Q, Sun J-K, Long D-H, Dong H, Sun L-T, Zhong X-H, Wan L-J (2016) Zn-Cu-In-Se quantum dot solar cells with a certified power conversion efficiency of 11.6%. J Am Chem Soc 138:4201–4209

6. Zhao K, Pan Z-X, Mora-Seró I, Wang H, Song Y, Gong X-Q, Wang J, Bonn M, Bisquert J, Zhong X-H (2015) Boosting power conversion efficiencies of quantum-dot-sensitized solar cells beyond 8% by recombination control. J Am Chem Soc 137:5602–5609

7. Ali M, Zhou F-L, Chen K, Kotzur C, Xiao C-L, Bourgeois L, Zhang X-Y, MacFarlane D-R (2016) Nanostructured photoelectrochemical solar cell for nitrogen reduction using plasmon-enhanced black silicon. Nat Commun 11335:1–5

8. Li Q-Y, Guan Z-P, Wu D, Zhao X-G, Bao S-Y, Tian B-Z, Zhang J-L (2017) Z-Scheme BiOCl-Au-CdS heterostructure with enhanced sunlight-driven photocatalytic activity in degrading water dyes and antibiotics. ACS Sustain Chem Eng 5:6958–6968

9. Li Q-Y, Li T-Y, Chang S-Z, Tao Q-S, Tian B-Z, Zhang J-L (2016) Enlarging {110} exposed facets of anatase TiO_2 by the synergistic action of capping agents. CrystEngComm 18:5074–5078

10. Li T-Y, Tian B-Z, Zhang J-L, Dong R-F, Wang T-T, Yang F (2013) Facile tailoring of anatase TiO_2 morphology by use of H_2O_2: from microflowers with dominant {101} facets to microspheres with exposed {001} facets. Ind Eng Chem Res 52(20):6704–6712

11. Weon S-H, Choi J-M, Park T-H, Choi W-Y (2017) Freestanding doubly open-ended TiO_2 nanotubes for efficient photocatalytic degradation of volatile organic compounds. Appl Catal B 205:386–392

12. Ren L, Li Y-Z, Hou J-T, Bai J-L, Mao M-Y, Zeng M, Zhao X-J, Li N (2016) The pivotal effect of the interaction between reactant and anatase TiO_2 nanosheets with exposed {001} facets on photocatalysis for the photocatalytic purification of VOCs. Appl Catal B 181:625–634

13. Wu D, Yue S-T, Wang W, An T-C, Li G-Y, Yip H-Y, Zhao H-J, Wong P-K (2016) Boron doped BiOBr nanosheets with enhanced photocatalytic inactivation of Escherichia coli. Appl Catal B 192:35–45

14. Wang W-J, An T-C, Li G-Y, Xia D-H, Zhao H-J, Yu J-C, Wong P-K (2017) Earth-abundant Ni_2P/g-C_3N_4 lamellar nanohydrids for enhanced photocatalytic hydrogen evolution and bacterial inactivation under visible light irradiation. Appl Catal B 217:570–580

15. Rtimi S, Giannakis S, Sanjines R, Pulgarin C, Bensimon M, Kiwi J (2016) Insight on the photocatalytic bacterial inactivation by co-sputtered TiO_2-Cu in aerobic and anaerobic conditions. Appl Catal B 182:277–285

16. Kuehnel M-F, Orchard K-L, Dalle K-E, Reisner E (2017) Selective photocatalytic CO_2 reduction in water through anchoring of a molecular Ni catalyst on CdS nanocrystals. J Am Chem Soc 139:7217–7223

17. Takeda H, Ohashi K, Sekine A, Ishitani O (2016) Photocatalytic CO_2 reduction using Cu (I) photosensitizers with a Fe(II) catalyst. J Am Chem Soc 138:4354–4357

18. Dong C-Y, Xing M-Y, Zhang J-L (2016) Double-cocatalysts promote charge separation efficiency in CO_2 photoreduction: spatial location matters. Mater Horiz 3:608–612

19. Dong C-Y, Xing M-Y, Zhang J-L (2016) Economic hydrophobicity triggering of CO_2 photoreduction for selective CH_4 generation on noble-metal-free TiO_2–SiO_2. J Phys Chem Lett 7:2962–2966

20. Fang W-Z, Dappozze F, Guillard C, Zhou Y, Xing M-Y, Mishra S, Daniele S, Zhang J-L (2017) Zn-assisted TiO_{2-x} photocatalyst with efficient charge separation for enhanced photocatalytic activities. J Phys Chem C 121:17068–17076

21. Schneider J, Matsuoka M, Takeuchi M, Zhang J-L, Horiuchi Y, Anpo M, Bahnemann D-W (2014) Understanding TiO_2 photocatalysis: mechanisms and materials. Chem Rev 114:9919–9986

22. Qiu B-C, Xing M-Y, Zhang J-L (2014) Mesoporous TiO_2 nanocrystals grown in situ on graphene aerogels for high photocatalysis and lithium-ion batteries. J Am Chem Soc 136:5852–5855

23. Qi D-Y, Lu L-J, Wang L-Z, Zhang J-L (2014) Improved SERS sensitivity on plasmon-free TiO_2 photonic microarray by enhancing light-matter coupling. J Am Chem Soc 136:9886–9889

24. Li X, Liu P-W, Mao Y, Xing M-Y, Zhang J-L (2015) Preparation of homogeneous nitrogen-doped mesoporous TiO_2 spheres with enhanced visible-light photocatalysis. Appl Catal B 164:352–359

25. Tani T (1995) Photographic sensitivity theory and mechanisms. Oxford University Press, New York
26. Tian B-Z, Zhang J-L (2012) Morphology-controlled synthesis and applications of silver halide photocatalytic materials. Catal Surv Jpn 16:210–230
27. Tani T (2011) Photographic sensitivity advances in nanoparticles, J-aggregates, dye sensitization, and organic devices. Oxford University Press, Oxford/New York
28. Cox R-J (1973) Photographic sensitivity. Academic Press Inc (London) LT, London
29. Kakuta N, Goto N, Ohkita H, Mizushima T (1999) Silver bromide as a photocatalyst for hydrogen generation from CH_3OH/H_2O solution. J Phys Chem B 103:5917–5919
30. Schürch D, Currao A, Sarkar S, Hodes G, Calzaferri G (2002) The silver chloride photoanode in photoelectrochemical water splitting. J Phys Chem B 106:12764–12775
31. Pfanner K, Gfeller N, Calzaferri G (1996) Photochemical oxidation of water with thin AgCl layers. J Photochem Photobiol A 95:175–180
32. Hu C, Lan Y-Q, Qu J-H, Hu X-X, Wang A-M (2006) $Ag/AgBr/TiO_2$ visible light photocatalyst for destruction of azodyes and bacteria. J Phys Chem B 110:4066–4072
33. Wang P, Huang B-B, Qin X-Y, Zhang X-Y, Dai Y, Wei J-Y, Whangbo M-H (2008) Ag@AgCl: a highly efficient and stable photocatalyst active under visible light. Angew Chem Int Ed 47:7931–7933
34. Wikipedia. www.en.wikipedia.org
35. Tian B-Z, Dong R-F, Zhang J-M, Bao S-Y, Yang F, Zhang J-L (2014) Sandwich-structured $AgCl@Ag@TiO_2$ with excellent visible-light photocatalytic activity for organic pollution degradation and E. coli K12 inactivation. Appl Catal B 158−159:76–84
36. Bao S-Y, Wang Z-Q, Gong X-Q, Zeng C-Y, Wu Q-F, Tian B-Z, Zhang J-L (2016) AgBr tetradecahedrons with co-exposed {100} and {111} facets: simple fabrication and enhancing spatial charge separation using facet heterojunction. J Mater Chem A 4:18570–18577
37. Lin H-L, Cao J, Luo B-D, Xu B-Y, Chen S-F (2012) Synthesis of novel Z-scheme AgI/Ag/AgBr composite with enhanced visible light photocatalytic activity. Catal Commun 21:91–95
38. Tao Q-S, Yang F, Teng F, Wu P-Y, Tian B-Z, Zhang J-L (2015) Study of the factors influencing the photo-stability of Ag@AgBr plasmonic photocatalyst. Res Chem Intermed 41:7285–7297
39. Zeng C-Y, Guo M, Tian B-Z, Zhang J-L (2013) Reduced graphene oxide modified Ag/AgBr with enhanced visible light photocatalytic activity for methyl orange degradation. Chem Phys Lett 575:81–85
40. Zhu J, Li C-J, Teng F, Tian B-Z, Zhang J-L (2015) Recyclable Ag@AgBr-gelatin film with superior visible-light photocatalytic activity for organic degradation. Res Chem Intermed 41:9715–9730
41. Dong R-F, Tian B-Z, Zeng C-Y, Li T-Y, Wang T-T, Zhang J-L (2013) Ecofriendly synthesis and photocatalytic activity of uniform cubic Ag@AgCl plasmonic photocatayst. J Phys Chem C 117:213–220
42. Zeng C-Y, Tian B-Z, Zhang J-L (2013) Silver halide/silver iodide@silver composite with excellent visible light photocatalytic activity for methyl orange degradation. J Colloid Interface Sci 405:17–21
43. Dong R-F, Tian B-Z, Zhang J-L, Wang T-T, Tao Q-S, Bao S-Y, Yang F, Zeng C-Y (2013) $AgBr@Ag/TiO_2$ core-shell composite with excellent visible light photocatalytic activity and hydrothermal stability. Catal Commun 38:16–20
44. Zhang P, Wu P-Y, Bao S-Y, Wang Z, Tian B-Z, Zhang J-L (2016) Synthesis of sandwich-structured $AgBr@Ag@TiO_2$ composite photocatalyst and study of its photocatalytic performance for the oxidation of benzyl alcohols to benzaldehydes. Chem Eng J 306:1151–1161
45. Yang F, Tian B-Z, Zhang J-L, Xiong T-Q, Wang T-T (2014) Preparation, characterization, and photocatalytic activity of porous AgBr@Ag and AgBrI@Ag plasmonic photocatalysts. Appl Surf Sci 292:256–261
46. Bi Y-P, Ye J-H (2010) Direct conversion of commercial silver foils into high aspect ratio AgBr nanowires with enhanced photocatalytic properties. Chem Eur J 16:10327–10331

47. Cao Q, Liu X, Yuan K-P, Yu J, Liu Q-H, Delaunay J-J, Che R (2017) Gold nanoparticled decorated Ag(Cl, Br) micro-necklaces for efficient and stable SERS detection and visible-light photocatalytic degradation of Sudan I. Appl Catal B 201:607–616

48. Bi Y-P, Ye J-H (2009) In situ oxidation synthesis of Ag/AgCl core-shell nanowires and their photocatalytic properties. Chem Commun 43:6551–6553

49. Bi Y-P, Ye J-H (2010) Heteroepitaxial growth of platinum nanocrystals on AgCl nanotubes via galvanic replacement reaction. Chem Commun 46:1532–1534

50. Jia C-C, Yang P, Huang B-B (2014) Uniform Ag/AgCl necklace-like nano-heterostructures: fabrication and highly efficient plasmonic photocatalysis. ChemCatChem 6:611–617

51. Ge J, Wang X, Yao H-B, Zhu H-W, Peng Y-C, Yu S-H (2015) Durable Ag/AgCl nanowires assembled in a sponge for continuous water purification under sunlight. Mater Horiz 2:509–513

52. Sun Y-G (2010) Conversion of Ag nanowires to AgCl nanowires decorated with Au nanoparticles and their photocatalytic activity. J Phys Chem C 114:2127–2133

53. Zhu M-S, Chen P-L, Liu M-H (2012) Highly efficient visible-light-driven plasmonic photocatalysts based on graphene oxide-hybridized one-dimensional Ag/AgCl heteroarchitectures. J Mater Chem 22:21487–21494

54. Sun L, Zhang R-Z, Wang Y, Chen W (2014) Plasmonic Ag@AgCl nanotubes fabricated from copper nanowires as high-performance visible light photocatalyst. ACS Appl Mater Interfaces 6:14819–14826

55. Li B, Wang H, Zhang B-W, Hu P-F, Chen C, Guo L (2013) Facile synthesis of one dimensional AgBr@Ag nanostructures and their visible light photocatalytic properties. ACS Appl Mater Interfaces 5:12283–12287

56. Chen D-L, Liu M-N, Chen Q-Q, Ge L-F, Fan B-B, Wang H-L, Lu H-X, Yang D-Y, Zhang R, Yan Q-S, Shao G-S, Sun J, Gao L (2014) Large-scale synthesis and enhanced visible-light-driven photocatalytic performance of hierarchical Ag/AgCl nanocrystals derived from freeze-dried PVP-Ag$^+$ hybrid precursors with porosity. Appl Catal B 144:394–407

57. Ai L-H, Zhang C-H, Jiang J (2013) Hierarchical porous AgCl@Ag hollow architectures: self-templating synthesis and highly enhanced visible light photocatalytic activity. Appl Catal B 142−143:744–751

58. Tang Y-X, Jiang Z-L, Xing G-C, Li A-R, Kanhere P-D, Zhang Y-Y, Sum T-C, Li S-Z, Chen X-D, Dong Z-L, Chen Z (2013) Efficient Ag@AgCl cubic cage photocatalysts profitfrom ultrafast plasmon-induced electron transfer processes. Adv Funct Mater 23:2932–2940

59. Li H-Y, Wu T-S, Cai B, Ma W-G, Sun Y-J, Gan S-Y, Han D-X, Niu L (2015) Efficiently photocatalytic reduction of carcinogenic contaminant Cr(VI) upon robust AgCl:Ag hollow nanocrystals. Appl Catal B 164:344–351

60. Han C-C, Ge L, Chen C-F, Li Y-J, Zhao Z, Xiao X-L, Li Z-L, Zhang J-L (2014) Site-selected synthesis of novel Ag@AgCl nanoframes with efficient visible light induced photocatalytic activity. J Mater Chem A 2:12594–12600

61. Xiao X-L, Ge L, Han C-C, Li Y-J, Zhao Z, Xin Y-J, Fang S-M, Wu L-N, Qiu P (2015) A facile way to synthesize Ag@AgBr cubic cages with efficient visible-light-induced photocatalytic activity. Appl Catal B 163:64–572

62. Lou S-Y, Jia X-B, Wang Y-Q, Zhou S-M (2015) Template-assisted in-situ synthesis of porous AgBr/Ag composite microspheres as highly efficient visible-light photocatalyst. Appl Catal B 176–177:586–593

63. Kim J-W, Agesen L-K, Choi J-H, Choi J, Kim H-S, Liu J-Y, Cho C-R, Kang J-G, Ramazane A, Thornton K, Braun P-V (2015) Template-directed directionally solidified 3D mesostructured AgCl–KCl eutectic photonic crystals. Adv Mater 27:4551–4559

64. Wu S-K, Shen X-P, Ji Z-Y, Zhu G-X, Chen C-J, Chen K-M, Bu R, Yang L-M (2015) Synthesis of AgCl hollow cubes and their application in photocatalytic degradation of organic pollutants. CrystEngComm 17:2517–2522

65. Zhu M-S, Chen P-L, Liu M-H (2013) High-performance visible-light-driven plasmonic photocatalysts Ag/AgCl with controlled size and shape using graphene oxide as capping agent and catalyst promoter. Langmuir 29:9259–9268

66. Shahzad A, Kim W-S, Yu T (2016) A facile synthesis of Ag/AgCl hybrid nanostructures with tunable morphologies and compositions as advanced visible light plasmonic photocatalysts. Dalton Trans 45:9158–9165

67. Wang H, Li Y, Li C, He L, Guo L (2012) Facile synthesis of AgBr nanocubes for highly efficient visible light photocatalysts. CrystEngComm 14:7563–7566

68. An C-H, Peng S, Sun Y-G (2010) Facile synthesis of sunlight-driven AgCl:Ag plasmonic nanophotocatalyst. Adv Mater 22:2570–2574

69. Zhu M-S, Chen P-L, Ma W-H, Lei B, Liu M-H (2012) Template-free synthesis of cube-like Ag/AgCl nanostructures via a direct-precipitation protocol: highly efficient sunlight-driven plasmonic photocatalysts. ACS Appl Mater Interfaces 4:6386–6392

70. Han L, Wang P, Zhu C-Z, Zhai Y-M, Dong S-J (2011) Facile solvothermal synthesis of cube-like Ag@AgCl: a highly efficient visible light photocatalyst. Nanoscale 3:2931–2935

71. Chen D-L, Yoo S-H, Huang Q-S, Ali G, Cho S-O (2012) Sonochemical synthesis of Ag/AgCl nanocubes and their efficient visible-light-driven photocatalytic performance. Chem Eur J 18:5192–5200

72. Wang H, Gao J, Guo T-Q, Wang R-M, Guo L, Liu Y, Li J-L (2012) Facile synthesis of AgBr nanoplates with exposed {111} facets and enhanced photocatalytic properties. Chem Commun 48:275–277

73. Shen Y-F, Chen P-L, Xiao D, Chen C-C, Zhu M-S, Li T-S, Ma W-G, Liu M-H (2015) Spherical and sheetlike Ag/AgCl nanostructures: interesting photocatalysts with unusual facet-dependent yet substrate-sensitive reactivity. Langmuir 31:602–610

74. Lou Z-Z, Huang B-B, Qin X-Y, Zhang X-Y, Wang Z-Y, Zheng Z-K, Cheng H-F, Wang P, Dai Y (2011) One-step synthesis of AgBr microcrystals with different morphologies by ILs-assisted hydrothermal method. CrystEngComm 13:1789–1793

75. Zhang H-B, Lu Y-G, Liu H, Fang J-Z (2015) One-pot synthesis of high-index faceted AgCl nanocrystals with trapezohedral, concave hexoctahedral structures and their photocatalytic activity. Nanoscale 7:11591–11601

76. Moniz S-J-A, Shevlin S-A, Martin D-J, Guo Z-X, Tang J-W (2015) Visible-light driven heterojunction photocatalysts for water splitting-a critical review. Energy Environ Sci 8:731–759

77. Cheng H-F, Wang W-J, Huang B-B, Wang Z-Y, Zhan J, Qin X-Y, Zhang X-Y, Dai Y (2013) Tailoring AgI nanoparticles for the assembly of AgI/BiOI hierarchical hybrids with size-dependent photocatalytic activities. J Mater Chem A 1:7131–7136

78. Chen L-L, Jiang D-L, He T, Wu Z-D, Chen M (2013) In-situ ion exchange synthesis of hierarchical AgI/BiOI microsphere photocatalyst with enhanced photocatalytic properties. CrystEngComm 15:7556–7563

79. An C-H, Jiang W, Wang J-Z, Wang S-T, Ma Z-Z, Li Y-P (2013) Synthesis of three-dimensional AgI@TiO$_2$ nanoparticles with improved photocatalytic performance. Dalton Trans 42:8796–8801

80. Wu D-Y, Long M-C (2011) Realizing visible-light-induced self-cleaning property of cotton through coating N-TiO$_2$ film and loading AgI particles. ACS Appl Mater Interfaces 3:4770–4774

81. Song J-M, Zhang J, Ni J-J, Niu H-L, Mao C-J, Zhang S-Y, Shen Y-H (2014) One-pot synthesis of ZnO decorated with AgBr nanoparticles and its enhanced photocatalytic properties. CrystEngComm 16:2652–2659

82. Wang D-J, Guo L, Zhen Y-Z, Yue L-L, Xue G-L, Fu F (2014) AgBr quantum dots decorated mesoporous Bi$_2$WO$_6$ architectures with enhanced photocatalytic activities for methylene blue. J Mater Chem A 2:11716–11727

83. Xu H, Xu Y-G, Li H-M, Xia J-X, Xiong J, Yin S, Huang C-J, Wan H-L (2012) Synthesis, characterization and photocatalytic property of AgBr/BiPO₄ heterojunction photocatalyst. Dalton Trans 41:3387–3394

84. Wang D-W, Li Y, Puma G-L, Wang C, Wang P-F, Zhang W-L, Wang Q (2015) Dye-sensitized photoelectrochemical cell on plasmonic Ag/AgCl@chiral TiO₂ nanofibers for treatment of urban wastewater effluents, with simultaneous production of hydrogen and electricity. Appl Catal B 168−169:25–32

85. Andersson M, Birkedal H, Franklin N-R, Ostomel T, Boettcher S, Palmqyist A-E-C, Stucky G-D (2005) Ag/AgCl-loaded ordered mesoporous anatase for photocatalysis. Chem Mater 17:1409–1415

86. Hayashido Y, Naya S, Tada H (2016) Local electric field-enhanced plasmonic photocatalyst: formation of Ag cluster-incorporated AgBr nanoparticles on TiO₂. J Phys Chem C 120:19663–19669

87. Wang P-H, Tang Y-X, Dong Z-L, Chen Z, Lim T-T (2013) Ag–AgBr/TiO₂/RGO nanocomposite for visible-light photocatalytic degradation of penicillin G. J Mater Chem A 1:4718–4727

88. Elahifard M-R, Rahimnejad S, Haghighi S, Gholami M-R (2007) Apatite-coated Ag/AgBr/TiO₂ visible-light photocatalyst for destruction of bacteria. J Am Chem Soc 129:9552–9553

89. Xu Y-S, Zhang W-D (2013) Ag/AgBr-grafted graphite-like carbon nitride with enhanced plasmonic photocatalytic activity under visible light. ChemCatChem 5:2343–2351

90. Putri L-K, Ong W-J, Chang W-S, Chai S-P (2016) Enhancement in the photocatalytic activity of carbon nitride through hybridization with light sensitive AgCl for carbon dioxide reduction to methane. Cat Sci Technol 6:744–754

91. Zhang S-W, Li J-X, Wang X-K, Huang Y-S, Zeng M-Y, Xu J-Z (2014) In situ ion exchange synthesis of strongly coupled Ag@AgCl/g-C₃N₄ porous nanosheets as plasmonic photocatalyst for highly efficient visible-light photocatalysis. ACS Appl Mater Interfaces 6:22116–22125

92. Yao X-X, Liu X-H, Hu X-L (2014) Synthesis of the Ag/AgCl/g-C₃N₄ composite with high photocatalytic activity under visible light irradiation. ChemCatChem 6:3409–3418

93. Li H-Y, Gan S-Y, Wang H-Y, Han D-X, Niu L (2015) Intercorrelated Superhybrid of AgBr supported on graphitic-C₃N₄-decorated nitrogen-doped graphene: high engineering photocatalytic activities for water purification and CO₂ reduction. Adv Mater 27:6906–6913

94. Chen D-M, Wang Z-H, Du Y, Yang G-L, Ren T-Z, Ding H (2015) In situ ionic-liquid-assisted synthesis of plasmonic photocatalyst Ag/AgBr/g-C₃N₄ with enhanced visible-light photocatalytic activity. Catal Today 258:41–48

95. Jiang J, Zhao K, Xiao X-Y, Zhang L-Z (2012) Synthesis and facet-dependent photoreactivity of BiOCl single-crystalline nanosheets. J Am Chem Soc 134:4473–4476

96. Ye L-Q, Zhan L, Tian L-H, Peng T-Y, Zhang J-J (2011) The {001} facets-dependent high photoactivity of BiOCl nanosheets. Chem Commun 47:6951–6953

97. Li H, Shang J, Ai Z, Zhang L-Z (2015) Efficient visible light nitrogen fixation with BiOBr nanosheets of oxygen vacancies on the exposed {001} facets. J Am Chem Soc 137:6393–6399

98. Cheng H-F, Huang B-B, Dai Y (2014) Engineering BiOX (X=Cl, Br, I) nanostructures for highly efficient photocatalytic applications. Nanoscale 6:2009–2026

99. Cheng H-F, Huang B-B, Dai Y, Qin X-Y, Zhang X-Y (2010) One-step synthesis of the nanostructured AgI/BiOI composites with highly enhanced visible-light photocatalytic performances. Langmuir 26(9):6618–6624

100. Cheng H-F, Huang B-B, Wang P, Wang Z-Y, Lou Z-Z, Wang J-P, Qin X-Y, Zhang X-Y, Dai Y (2011) In situ ion exchange synthesis of the novel Ag/AgBr/BiOBr hybrid with highly efficient decontamination of pollutants. Chem Commun 47:7054–7056

101. Ye L-Q, Liu J-Y, Gong C-Q, Tian L-H, Peng T-Y, Zan L (2012) Two different roles of metallic Ag on Ag/AgX/BiOX (X=Cl, Br) visible light photocatalysts: surface plasmon resonance and Z-scheme bridge. ACS Catal 2:1677–1683

102. Xiong W, Zhao Q-D, Li X-Y, Zhang D-K (2011) One-step synthesis of flower-like Ag/AgCl/BiOCl composite with enhanced visible-light photocatalytic activity. Catal Commun 16:229–233

103. Kong L, Jiang Z, Lai H-H, Nicholls R-J, Xiao T-C, Jones M-O, Edwards P-P (2012) Unusual reactivity of visible-light-responsive AgBr-BiOBr heterojunction photocatalysts. J Catal 293:116–125

104. Wang W-S, Du H, Wang R-X, Wen T, Xu A-W (2013) Heterostructured Ag_3PO_4/AgBr/Ag plasmonic photocatalyst with enhanced photocatalytic activity and stability under visible light. Nanoscale 5:3315–3321

105. Yang S-B, Xu D-B, Chen B-Y, Luo B-F, Shi W-D (2017) In-situ synthesis of a plasmonic Ag/AgCl/Ag_2O heterostructures for degradation of ciprofloxacin. Appl Catal B 204:602–610

106. Sang Y, Kuai L, Chen C-Y, Fang Z, Geng B-Y (2014) Fabrication of a visible-light-driven plasmonic photocatalyst of $AgVO_3$@AgBr@Ag nanobelt heterostructures. ACS Appl Mater Interfaces 6:5061–5068

107. Zhang A-C, Zhang L-X, Lu H, Chen G-Y, Liu Z-C, Xiang J, Sun L-S (2016) Facile synthesis of ternary Ag/AgBr-Ag_2CO_3 hybrids with enhanced photocatalytic removal of elemental mercury driven by visible light. J Hazar Mater 314:78–87

108. Bao S-Y, Wu Q-F, Chang S-Z, Tian B-Z, Zhang J-L (2017) Z-scheme CdS-Au-$BiVO_4$ with enhanced photocatalytic activity for organic contaminant decomposition. Cat Sci Technol 7:124–132

109. Tada H, Mitsui T, Kiyonaga T, Akita T, Tanaka K (2006) All-solid-state Z-scheme in CdS–Au–TiO_2 three-component nanojunction system. Nat Mater 5:782–786

110. Wang X-W, Liu G, Wang L-Z, Chen Z-G, Lu G-Q, Cheng H-M (2012) ZnO-CdS@Cd heterostructure for effective photocatalytic hydrogen generation. Adv Energy Mater 2:42–46

111. Zhou P, Yu J-G, Jaroniec M (2014) All-solid-state Z-scheme photocatalytic systems. Adv Mater 26:4920–4935

112. Iwase A, Ng Y-H, Ishiguro Y, Kudo A, Amal R (2011) Reduced graphene oxide as a solid-state electron mediator in Z-scheme photocatalytic water splitting under visible light. J Am Chem Soc 133:11054–11057

113. Maeda K (2013) Z-scheme water splitting using two different semiconductor photocatalysts. ACS Catal 3:1486–1503

114. Li H-Y, Sun Y-J, Cai B, Gan S-Y, Han D-X, Niu L, Wu T-S (2015) Hierarchically Z-scheme photocatalyst of Ag@AgCl decorated on $BiVO_4$ (040) with enhancing photoelectrochemical and photocatalytic performance. Appl Catal B 170−171:206–214

115. Qiao R, Mao M-M, Hu E-L, Zhong Y-J, Ning J-Q, Hu Y (2015) Facile formation of mesoporous $BiVO_4$/Ag/AgCl heterostructured microspheres with enhanced visible-light photoactivity. Inorg Chem 54:9033–9039

116. Zhang J, Niu C-G, Ke J, Zhou L-F, Zeng G-M (2015) Ag/AgCl/Bi_2MoO_6 composite nanosheets: a plasmonic Z-scheme visible light photocatalyst. Catal Commun 59:30–34

117. Hou J-G, Wang Z, Yang C, Zhou W-L, Jiao S-Q, Zhu H-M (2013) Hierarchically plasmonic Z-scheme photocatalyst of Ag/AgCl nanocrystals decorated mesoporous single-crystalline metastable $Bi_{20}TiO_{32}$ nanosheets. J Phys Chem C 117:5132–5141

118. Hou J-G, Yang C, Wang Z, Ji Q-H, Li Y-T, Huang G-C, Jiao S-Q, Zhu H-M (2013) Three-dimensional Z-scheme AgCl/Ag/γ-TaON heterostructural hollow spheres for enhanced visible-light photocatalytic performance. Appl Catal B 142−143:579–589

119. Wang X-F, Li S-F, Ma Y-Q, Yu H-G, Yu J-G (2011) $H_2WO_4 \cdot H_2O$/Ag/AgCl composite nanoplates: a plasmonic Z-scheme visible-light photocatalyst. J Phys Chem C 115:14648–14655

120. Yao X-X, Liu X-H (2014) One-pot synthesis of ternary Ag_2CO_3/Ag/AgCl photocatalyst in natural geothermal water with enhanced photocatalytic activity under visible light irradiation. J Hazard Mater 280:260–268

121. Cheng H-J, Hou J-G, Zhu H-M, Guo X-M (2014) Plasmonic Z-scheme α/β-Bi$_2$O$_3$-Ag-AgCl photocatalyst with enhanced visible-light photocatalytic performance. RSC Adv 4:41622–41630

122. Zhou T, Xu Y-G, Xu H, Wang H-F, Da Z-L, Huang S-Q, Ji H-Y, Li H-M (2014) In situ oxidation synthesis of visible-light-driven plasmonic photocatalyst Ag/AgCl/g-C$_3$N$_4$ and its activity. Ceram Int 40:9293–9301

123. Yan X, Wang X-Y, Gu W, Wu M-M, Yan Y, Hu B, Che G-B, Han D-L, Yang J-H, Fan W-Q, Shi W-D (2015) Single-crystalline AgIn(MoO$_4$)$_2$ nanosheets grafted Ag/AgBr composites with enhanced plasmonic phtotcatalytic activity for degradation of tetracycline under visible light. Appl Catal B 164:297–304

124. Wang X-H, Yang J, Ma S-Q, Zhao D, Dai J, Zhang D-F (2016) In situ fabrication of AgI/AgVO$_3$ nanoribbon composites with enhanced visible photocatalytic activity for redox reactions. Cat Sci Technol 6:243–253

125. Li J-J, Xie Y-L, Zhong Y-J, Hu Y (2015) Facile synthesis of Z-scheme Ag$_2$CO$_3$/Ag/AgBr ternary heterostructured nanorods with improved photostability and photoactivity. J Mater Chem A 3:5474–5481

126. Zhang L-S, Wong K-H, Chen Z-G, Yu J-C, Zhao J-C, Hu C, Chan C-Y, Wong P-K (2009) AgBr-Ag-Bi$_2$WO$_6$ nanojunction system: a novel and efficient photocatalyst with double visible-light active components. Appl Catal A General 363:221–229

127. Katsumata H, Hayashi T, Taniguchi M, Suzuki T, Kaneco S (2014) Highly efficient visible-light driven AgBr/Ag$_3$PO$_4$ hybrid photocatalysts with enhanced photocatalytic activity. Mater Sci Semicond Process 25:68–75

128. Cao J, Zhao Y-J, Lin H-L, Xu B-Y, Chen S-F (2013) Facile synthesis of novel Ag/AgI/BiOI composites with highly enhanced visible light photocatalytic performances. J Solid State Chem 206:38–44

129. Xie R-Y, Zhang L-P, Xu H, Zhong Y, Sui X-F, Mao Z-P (2015) Fabrication of Z-scheme photocatalyst Ag-AgBr@Bi$_{20}$TiO$_{32}$ and its visible-light photocatalytic activity for the degradation of isoproturon herbicide. J Mol Catal A Chem 406:194–203

130. Yang Y-X, Wan G, Guo Y-N, Zhao Y-H, Yuan X, Guo Y-H (2014) Fabrication of Z-scheme plasmonic photocatalyst Ag@AgBr/g-C$_3$N$_4$ with enhanced visible-light photocatalytic activity. J Hazard Mater 271:150–159

131. Tian B-Z, Wang T-T, Dong R-F, Bao S-Y, Yang F, Zhang J-L (2014) Core-shell structured γ-Fe$_2$O$_3$@SiO$_2$@AgBr:Ag composite with high magnetic separation efficiency and excellent visible light activity for acid orange 7 degradation. Appl Catal B 147:22–28

132. Xia D-H, Hu L-L, Tan X-Q, He C, Pan W-Q, Yang T-S, Huang Y-L, Shu D (2016) Immobilization of self-stabilized plasmonic Ag-AgI on mesoporous Al$_2$O$_3$ for efficient purification of industrial waste gas with indoor LED illumination. Appl Catal B 185:295–306

133. Fan Y-Y, Ma W-G, Han D-X, Gan S-Y, Dong X-D, Niu L (2015) Convenient recycling of 3D AgX/Graphene aerogels (X= Br, Cl) for efficient photocatalytic degradation of water pollutants. Adv Mater 27:3767–3773

134. Xu Y-G, Zhou T, Huang S-Q, Xie M, Li H-P, Xu H, Xia J-X, Li H-M (2015) Preparation of magnetic Ag/AgCl/CoFe$_2$O$_4$ composites with high photocatalytic and antibacterial ability. RSC Adv 5:41475–41483

135. Jing L-Q, Xu Y-G, Huang S-Q, Xie M, He M-Q, Xu H, Li H-M, Zhang Q (2016) Novel magnetic CoFe$_2$O$_4$/Ag/Ag$_3$VO$_4$ composites: highly efficient visible light photocatalytic and antibacterial activity. Appl Catal B 199:11–22

136. Li Z-L, Ai J-Z, Ge M (2017) A facile approach assembled magnetic CoFe$_2$O$_4$/AgBr composite for dye degradation under visible light. J Environ Chem Eng 5:1394–1403

137. An C-H, Ming X-J, Wang J-Z, Wang S-T (2012) Construction of magnetic visible-light-driven plasmonic Fe$_3$O$_4$@SiO$_2$@AgCl:Ag nanophotocatalyst. J Mater Chem 22:5171–5176

138. Guo J-F, Ma B-W, Yin A-Y, Fan K-N, Dai W-L (2011) Photodegradation of rhodamine B and 4-chlorophenol using plasmonic photocatalyst of Ag-AgI/Fe$_3$O$_4$@SiO$_2$ magnetic nanoparticle under visible light irradiation. Appl Catal B 101:580–586

139. Li G-T, Wong K-H, Zhang X-W, Hu C, Yu J-C, Chan R-C-Y, Wong P-K (2009) Degradation of Acid Orange 7 using magnetic AgBr under visible light: the roles of oxidizing species. Chemosphere 76:1185–1191
140. Huang S-Q, Xu Y-G, Chen Z-G, Xie M, Xu H, He M-Q, Li H-M, Zhang Q (2015) A core-shell structured magnetic Ag/AgBr@Fe$_2$O$_3$ composite with enhanced photocatalytic activity for organic pollutant degradation and antibacterium. RSC Adv 5:71035–71045
141. Zhao H-H, Zhang L-S, Gu X-D, Li S-J, Li B, Wang H-L, Yang J-M, Liu J-S (2015) Fe$_2$O$_3$-AgBr nonwoven cloth with hierarchical nanostructures as efficient and easily recyclable macroscale photocatalysts. RSC Adv 5:10951–10959
142. Xu Y-G, Huang S-Q, Xie M, Li Y-P, Jing L-Q, Xu H, Zhang Q, Li H-M (2016) Core-shell magnetic Ag/AgCl@Fe$_2$O$_3$ photocatalysts with enhanced photoactivity for eliminating bisphenol A and microbial contamination. New J Chem 40:3413–3422
143. McEvoy J-G, Zhang Z-S (2014) Synthesis and characterization of magnetically separable Ag/AgCl-magnetic activated carbon composites for visible light induced photocatalytic detoxification and disinfection. Appl Catal B 160–161:267–278